



University
of Glasgow | School of
Engineering

Mechanical Response of Permeable Concrete with Steel Fibres

Christopher Whitton

Abstract

In searching for effective methods for directing stormwater safely, permeable concrete has become significantly more popular in recent times. With a purposely high void content, permeable concrete is significantly weaker than conventional concrete and therefore, methods of improving the mechanical properties without disrupting the desirable permeability have been sought out.

A joint study has been undertaken on mixing steel fibres into the permeable concrete to determine the effects on the main mechanical properties and permeability. This paper focusses specifically on whether the mechanical properties are improved by the fibres and the potential of simulating plain and fibrous permeable concrete behaviour patterns with the CDPM2 concrete behaviour model. Conneely (2019) focusses on the permeability aspect of this study.

The study of the mechanical properties has been achieved by experimentally testing samples, with and without fibres, in compression and tensile splitting tests to determine the changes in the behavioural response parameters. These parameters have then been used as the basis for material inputs in a simulation model of the tensile splitting test. This simulation utilises a homogeneous mesh and the CDPM2 model which is optimised for conventional concrete.

The experimental results show that the fibres increase strength significantly in compression and slightly less so in tension. The stiffness of the permeable concrete is also increased, as is the resistance to crumbling and disintegration. The simulation results show that the load required for splitting failure can be reasonably estimated and that the standard CDPM2 behaviour model performed generally well against the compression test results during parameter determination. However, the tensile post-peak behaviour could not be accurately studied with the splitting test.

These results show that steel fibres significantly improve the mechanical behavioural properties of permeable concrete but, both experimentally and computationally, a different kind of tensile test would have to be undertaken to fully understand the tensile benefits and draw a complete and accurate tensile fracture response comparison.

In the context of the joint study, research from Conneely (2019) indicates that the fibres also increase the permeability as well as increasing the strength. Therefore, the overall conclusion is that the use of steel fibres in permeable concrete mixes is beneficial in optimising both the mechanical and permeability properties.

Contents

Abstract	ii
List of Symbols	v
Preface	viii
1 Introduction	1
1.1 Background	1
1.2 Aims and Objectives	2
1.3 Project Outline and Methods	2
1.3.1 General Outline	2
1.3.2 Specific Test Methods	3
2 Literature Review	4
2.1 Concrete Characteristics and Behaviour	4
2.1.1 Permeable Concrete	4
2.1.2 Behaviour of Fibre Reinforced Concrete	7
2.2 Testing of Concrete Properties	8
2.3 Modelling of Concrete Behaviour	10
2.4 Verification and Validation	12
3 Physical Experiments	13
3.1 Specimen Size and Number	13
3.2 Concrete Mix Design	13
3.3 Sample Preparation	14
3.3.1 Mixing and Compacting	14
3.3.2 Curing, Permeability Testing and Final Preparation	15
3.4 Concrete Testing	16
3.4.1 Compression Test	16
3.4.2 Tensile Splitting Test	21
4 Material Simulation Models	27
4.1 Modelling in Macroscale	27
4.2 Non-Linear Finite Element Method	27
4.3 CDPM2 Non-linear Finite Element Constitutive Model	27
4.3.1 Model Operation and Implementation	28
4.3.2 LSDYNA Constitutive Model - MAT_CDPM	31
4.4 Plywood Bearing Plates Linear Elastic Model	33
4.5 Explicit Analysis LS-DYNA Time Step Calculation	34
4.6 Displacement Load Definition	35
5 Simulation Analysis	36
5.1 Setup of Analysis	36

5.1.1 Modelling Strategy and Tensile Stress Calculation	36
5.1.2 Tensile Splitting Test Model geometry	36
5.1.3 Strip Contact Definition	37
5.1.4 Deriving Inputs for Permeable Concrete CDPM2 Behaviour Models	38
5.2 Set Specific Inputs, Results and Discussion.....	40
5.2.1 Set 1.....	40
5.2.2 Set 2.....	45
5.2.3 Set 3.....	48
5.2.4 Set 4.....	51
5.2.5 Permeable Concrete Results Summary.....	53
5.3 Model Validation and Objectivity of Results.....	53
5.3.1 Setup.....	54
5.3.2 Loading Results	55
5.3.3 Discussion.....	55
5.3.4 Validation and Objectivity Results Summary.....	57
6 Results in Relation to Permeability Investigation	59
6.1 Results.....	59
6.2 Discussion.....	60
7 Conclusions	61
8 Further Work	62
9 References	63
10 Appendices.....	68
Appendix A - Concrete Constituent Calculations.....	68
Appendix B - Tensile Splitting Test LS-DYNA code.....	72
B.1 - Tensile Splitting Test Input File.....	72
B.2 - Cylinder Mesh Input File.....	75
B.3 - Shell Loading Strips Input File.....	76

List of Symbols

Latin Lower-Case Symbols

c	-	Speed of sound in material
f_{bc}	-	Factor of compressive strength for eccentricity parameter calculation
f_c	-	Ultimate uniaxial compressive strength of concrete
f_t	-	Ultimate uniaxial tensile strength of concrete
f_{t1}	-	CDPM2 intermediate damage stress parameter in bilinear softening.
$f_{t,sp}$	-	Splitting test tensile strength
m_g	-	CDPM2 dilation variable
q_{h0}	-	CDPM2 initial Hardening Parameter
q_{h1}, q_{h2}	-	CDPM2 hardening variables
s_1, s_2, s_3	-	Deviatoric stresses
t	-	Timestep size
ν_c	-	Poisson's Ratio for concrete
ν_p	-	Poisson's Ratio for plywood
w_f	-	CDPM2 maximum tensile damage variable
w_{f1}	-	CDPM2 intermediate damage displacement parameter in bilinear softening
x_s	-	CDPM2 ductility measure

Latin Upper-Case Symbols

A_b	-	Area of one cube face in the compression test
A_h	-	CDPM2 hardening ductility parameter
A_s	-	CDPM2 ductility parameter during damage
B_h	-	CDPM2 hardening ductility parameter
B_s	-	CDPM2 damage ductility exponent during damage
C_h	-	CDPM2 hardening ductility parameter

D	-	Specimen Diameter
D_f	-	CDPM2 flow rule parameter
D_h	-	CDPM2 hardening ductility parameter
E_c	-	Concrete Young's Modulus
ECC	-	CDPM2 eccentricity parameter
E_p	-	Plywood Young's Modulus
F_c	-	Compressive force from loading plate
F_{c0}	-	CDPM2 rate Dependent Parameter
F_{max}	-	Maximum load applied to specimen
G_F	-	Crack release energy
h	-	CDPM2 mesh dependent strain-to-displacement conversion parameter
J_2, J_3	-	Stress invariants
L	-	Specimen Length
L_{cube}	-	Length of cube side
L_{el}	-	Discretised Element Length
L_{plate}	-	Displacement of loading plates

Greek Symbols

α_c	-	CDPM2 damage type predictor
α_{sp}	-	Conversion factor between uniaxial tensile strength and splitting test tensile strength
Δ	-	Change in value, prefix
ε	-	Strain
$\tilde{\varepsilon}$	-	Equivalent strain
ϵ	-	Intermediate parameter for eccentricity parameter calculation
ε_0	-	Strain threshold for damage

ε_{ave}	-	Bulk or average strain over entire material
ε_c	-	Compressive strain
ε_{fc}	-	CDPM2 compressive Softening Parameter
ε_t	-	Tensile strain, Inelastic tensile strain
$\bar{\theta}$	-	Lode angle
κ_p	-	CDPM2 hardening variable
ξ	-	Volumetric stress length Haigh-Westergaard co-ordinate axis
ρ	-	Deviatoric stress length Haigh-Westergaard co-ordinate axis
$\bar{\rho}$	-	Deviatoric effective stress norm
ρ_c	-	Concrete Bulk Density
ρ_p	-	Plywood bulk density
σ	-	CDPM2 stress tensor
$\sigma_1, \sigma_2, \sigma_3$	-	Principle stresses
σ_c	-	Compressive stress
$\bar{\sigma}_c$	-	Negative part of CDPM2 effective stress tensor σ
σ_t	-	Uniaxial tensile stress
$\bar{\sigma}_t$	-	Positive part of CDPM2 effective stress tensor σ
$\bar{\sigma}_v$	-	Volumetric effective stress
ϕ	-	Porosity as percentage
ϕ_v	-	Porosity as factor of total volume
ω_t, ω_c	-	CDPM2 scalar damage variables where a value of 0 corresponds to no damage and 1 corresponds to full damage.

Preface

This joint investigation comprises physical experiments and computational analysis with the goal of determining the potential of steel fibres for improving the mechanical response of permeable concrete without disrupting permeability. This paper specifically focusses on the mechanical response while the effects on permeability are investigated by Conneely (2019).

This project was undertaken at the University of Glasgow from August 2018 to January 2019 for the fulfilment of the individual final year project submission included in the MEng Civil Engineering with Architecture program.

In completing this project, I would like to thank all the supporters and contributors. Firstly, my main advisor, Dr Peter Grassl, for his insightful and knowledgeable feedback and support, my second advisor, Dr Thomas Shire, for his extra guidance and input, Ian Gardner and Robert Boyd for their assistance in mixing and testing the concrete samples, and finally, all my family and friends for their continuous encouragement.

1 Introduction

1.1 Background

As our built environment expands, the human impact on the natural landscape is ever increasing. A major issue concerning these impacts is the effect on stormwater runoff where large areas of impermeable pavement are either catching the water and causing significant puddling or rapidly depositing it into the natural drainage system, causing potentially damaging flash flooding. A rising solution to this problem is the use of permeable concrete that allows water to pass through large connected voids and provides more controllable drainage into the ground for most major rainfall events.

Permeable concrete is made from a combination of aggregate, cement and water. Compared to conventional concrete, the amount of fine aggregate is significantly reduced, or not used at all, to create voids between the aggregate particles. The goal being that these voids connect to form paths that water can travel through. As with normal concrete, the mix design can be altered to emphasise certain properties and ensure that the finished product is suitable for the design situation. In using permeable concrete, the strength is significantly reduced due to the high void content however this is offset by its advantageous drainage properties. The balance between strength and permeability is key as one must be sacrificed to gain the other and therefore, it makes sense to search for ways to optimise both characteristics by altering the constituents or improving the efficiency of the present mix properties. Incorporating steel fibres has been used as a method of improving the mechanical properties of conventional concrete but has not been studied in great detail for permeable concrete.

In terms of modelling permeable concrete behaviour, previous University of Glasgow studies such as McTaggart (2016) and Lockhart (2017) have so far focussed on the modelling of conventional concrete or reinforced conventional concrete respectively. More specifically, they have validated the use of the concrete model CDPM2 for modelling structural failure in these materials, but not permeable concrete. CDPM2 is a combined damage-plasticity model that is able to define the general failure behaviour of concrete. It can be used to simulate the response of many different types and strengths of conventional concrete with the alteration of the input parameters. However, conventional concrete can be described by an almost entirely filled, homogeneous matrix for which the model was designed whereas permeable concrete has many voids and exposed interfaces. Less attention has been given to whether CDPM2 can also be applied to simulate the potential failure response and properties of plain and fibrous permeable concrete, rather than resorting to complex microscale analyses. If this can be realised efficiently, optimisation of permeable concrete usage in construction projects may become more achievable.

1.2 Aims and Objectives

The overall aim of this project is to investigate how the mechanical properties of permeable concrete can be improved while maintaining its high permeability. This study will focus on determining changes in the mechanical response of permeable concrete when steel fibres are added to mixes of different aggregate sizes. A separate study, produced by Conneely (2019), will determine the extent of which this fibre addition alters concrete permeability for similar mixes. A comparison of both studies will determine whether a strength increase can be achieved without significant reduction of permeability and show if the addition of fibres is beneficial. Furthermore, a finite element model simulation will be created to investigate the applicability of using the concrete behaviour model CDPM2 with a simplified mesh for modelling permeable concrete.

1.3 Project Outline and Methods

1.3.1 General Outline

The project will revolve around characterising the material response and parameters of the plain and fibrous permeable concrete mixes from experimental testing. The results of these experiments will be initially used to gain insight into the behavioural changes when the constituent properties are altered. This will allow any positive or negative outcomes to be identified and an initial conclusion about the altered mechanical characteristics to be formulated. These results will form the basis of discussion when being compared with the permeability results and are presented in section 3.

Next, the individual parameters from the experimental testing will also be used in a simulation that utilises the CDPM2 model. Only a few input parameters can be effectively determined from the experiments, so this simulation will be used to determine if the damage model in its current state can still provide accurate response patterns when only the main inputs such as strength, stiffness and damage ductility are changed. The material model and software features are described in section 4 and the simulation strategy and results are presented in section 5. A full outline of the altered input parameters is given in section 5.1.4.

Finally, a short discussion will address whether the addition of fibres affects permeability as well as strength and combine results from Conneely (2019) to satisfy the overall aim of the project. This is presented in section 6.

1.3.2 Specific Test Methods

To define the main material properties experimentally, four different permeable concrete mix designs will be created with varying aggregate sizes and fibrous content. Three cubes of each mix will be subjected to standard compression tests and three cylinders of each mix will be subjected to tensile splitting tests. Load-displacement curves will be monitored for both types of test to give a range of common material parameters and crack patterns will be monitored for the splitting test.

A simulation of the tensile splitting test on LS-DYNA will then be created using the CDPM2 behaviour model. The analysis assumes a homogeneous material mesh such as would be the case for conventional concrete but with the input parameters from the permeable concrete experiments. This type of mesh is required for the effective use of CDPM2. The simulation will initially be used to determine a value for the uniaxial tensile strength of each mix which is a required material parameter input for the behaviour model. With this value and other parameters, the effectiveness and accuracy of the homogeneous mesh and CDPM2 combination can then be evaluated against the experimental tensile splitting test results. The simulation will also be further explored against typical responses, mesh dependency and time dependency so that the results and usefulness of the simulation itself can be interpreted.

2 Literature Review

In this literature review, the general background and theory regarding the behaviour of permeable concrete is covered in relation to concrete in general under testing. This is to highlight the differences between the two respective types in both composition and mechanical response. A summary of the behaviour of fibre reinforced concrete and an extension to previous studies of fibres in permeable concrete is also given with a view to gaining an insight on what the results of this study may present. Further information is given on the tensile splitting test that will be key to this study and a brief review of previous constitutive models for concrete behaviour will be presented with their characteristics and performance outlined. Finally, the importance of verification and validation to this project will be highlighted with regards to the simulation being created.

2.1 Concrete Characteristics and Behaviour

2.1.1 Permeable Concrete

Permeable concrete contains similar constituents to conventional concrete with cement, aggregates, water and sometimes chemical admixtures used to enhance beneficial properties such as workability. However, rather than using a mix of fine and coarse aggregates, the aggregates used are restricted to coarser grades to create a significant void content within the matrix. The water content also needs to be much more tightly controlled so that the mixture retains sufficient moulding capabilities. Tennis et al (2004) states that void contents of between 15 and 25 percent are generally targeted as this level can allow for enough water storage and permeability to withstand the majority of weather events while maintaining a sufficient level of strength. Permeability can vary depending on the ratios of constituents used but values from 2×10^{-3} m/s to 11.67×10^{-3} m/s are common (adapted from Tennis et al, 2004). The density of permeable concrete usually lies in the range of 1600 - 2000 kg/m³ (Tennis et al, 2004), compared to around 2400 kg/m³ for normal concrete (Bright and Roberts, 2010), although denser mixes have also been used.

The main technical issue with permeable concrete is the significant reduction in strength and potential variability of strengths between mixes due to the void presence. Numerous tests have shown that the general range of compressive strengths is between 3.5 MPa and 28 MPa (Tennis et al, 2004) which is quite wide but significantly lower than the range of conventional concrete where strengths can reach 90 MPa or higher. Splitting tensile strengths can fall to very low values of around 1 MPa as demonstrated by Care et al. (2018). Like conventional concrete, strength properties can be improved by lowering the aggregate-to-cement or water-to-cement ratios (Joshi and Dave, 2016), but the potential for this will be limited by other requirements such as workability.

For most types of conventional concrete, certain behavioural characteristics are well known. The tensile strength of concrete is far lower than the compressive strength with tensile behaviour far more brittle as well. Chen (2007) states that a uniaxial tensile strength, f_t , of 5-10% of the compressive strength, f_c , is generally normal. Studies such as Mahalingam and Mahalingam (2016) show that this range is potentially a little low for permeable concrete. For 4.75 - 9.5 mm aggregates with a 4:1 aggregate-to-cement mixing ratio, a value of 13% f_c is obtained for tensile strength. For slightly larger 9.5 - 12.5 mm aggregates, a value of nearly 15% f_c is recorded. The standards used for these tests were not British Standards so direct comparison is not necessarily achievable, but it can be noted that larger aggregate mixes have a higher tensile strength relative to the compressive strength than smaller aggregates in this investigation.

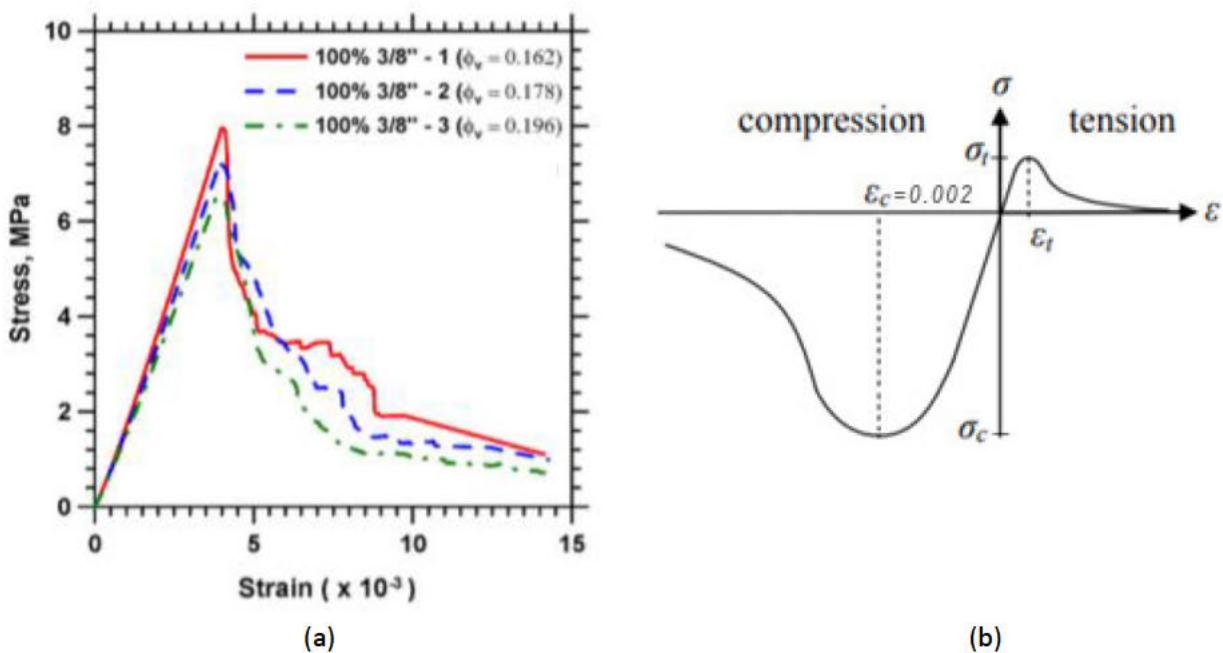


Figure 1: (a) Permeable Concrete Compressive Stress vs Strain Experimental Result from Deo and Neithalath (2010) and (b) Total standard description of concrete behaviour adapted from Nasset and Skoglund (2017)

Deo and Neithalath (2010) conducted a study on the compressive stress-strain response of permeable concrete for different porosities (denoted by ϕ_v as a factor of the total volume) and found that the general shape of the response curve in Figure 1(a) is relatively similar to conventional concrete, seen in Figure 1(b). The aggregate used for this particular response was 9.5 mm (or 3/8") and the aggregate-to-cement ratio employed was 5:1 but the porosity was varied between 0.162 and 0.196 of the total volume. Here, lower porosities are shown to give higher strengths.

A couple of significant differences can be noted from Figure 1(a) when compared against the traditional concrete loading response shown in Figure 1(b). The standard response for conventional concrete in compression is known to be caused by progression of microcracks with increasing loading (Chen, 2007) and this leads to the non-linear behaviour demonstrated by the curving of the stress response on the compression side. Microcracks initially form within the

concrete due to the processes of thermal expansion, drying shrinkage or constituent segregation. The weak bond between the aggregate and the cement allows differences in strains of the constituents to also form further microcracks when the specimen is loaded. In general, propagation of microcracks begins at around 30% of f_c and is stable until around 75% of f_c . Beyond 75%, the specimen becomes unstable and cracks continue to grow even if the loading is held steady. During failure, microcracks join and cause the stress capacity to drop indicating a softening response (Chen, 2007). In Figure 1(a), there appears to be very little non-linear behaviour before the peak stress is reached and this is shown as the case for all the aggregate types tested in Deo and Neithalath's investigation. The immediate stress decrease post-peak is also very steep and suggests rapid brittle failure in this region.

The strain at which the peak stress is recorded is increased in Figure 1(a) with failure occurring at around 0.004 strain rather than the 0.002 of normal concrete (Chen, 2007), indicating a more flexible material response up to failure. Initial post-peak behaviour can be seen in Figure 1(a) as strong softening with stresses rapidly dropping away with increasing strain. However, as with normal concrete, the gradient becomes less severe as the strain continues to rise. Another feature that is observed is the initial slight curve upwards indicating an increase in stiffness during early loading likely due to either light initial crushing of the material or the loading plates finding contact with protruding aggregates.

Complete tensile stress vs strain/displacement response studies of any kind for permeable concrete are scarce in literature. The studies that involved determination of tensile strength did not also include the response shape measured and only the final strength results were reported. In general, the standard response for conventional concrete in Figure 1(b) shows that failure in tension is much more brittle. There is significantly less non-linear behaviour before failure and nearing the tensile strength, propagating microcracks material again join and cause localised deformations (Chen, 2007). A drop in stress capacity is observed again but now, the failure stress is significantly lower. Given the overall similarities of the compression response shape to conventional concrete, the permeable concrete experiments will likely show a similar pattern. Rehder et al. (2014) has suggested that lower porosity increases the tensile load capacity of the specimen for given crack widths during post-peak loading.

Similar to normal concrete, post-peak behaviour of higher strength permeable concrete is more brittle with a steeper softening curve immediately after failure. This behaviour can be contrasted to the response of high-strength conventional concrete which includes admixtures such as microsilica, fly-ash and plasticisers to create mixes of very low void content and reduced crack mobility (Naik et al, 2012). This low void content increases the strength so in permeable concrete, the opposite happens when void content is increased.

Deo and Neithalath (2010) finds that larger aggregates may produce a wider range of results as the material structure is not as uniform and that strength capacity may be increased by mixing aggregate sizes together to improve homogeneity. It goes on to suggest that the recorded higher strength of coarser aggregates is caused by the lesser number of interacting pores and hence, potential areas for weaknesses in bonds during damage propagation are reduced. These weaknesses are further decreased due to the lower surface area of coarser aggregate and therefore, a thicker layer of cement paste can be distributed to each particle. However, there is some contention in these results as the mixes used a reduced level of cement and other studies, such as Mahalingam and Mahalingam (2016) and Joshi and Dave (2016), have found that smaller aggregate sizes lead to higher strengths. The strengths are not significantly different however so it does lead to the suggestion that aggregate sizes in the ranges tested may not have a huge effect on the overall strength properties.

2.1.2 Behaviour of Fibre Reinforced Concrete

As mentioned in section 2.1.1, concrete is weak in tension and also very brittle. Very low strain values can generate stresses sufficient to cause significant cracking within the concrete. Fibres can be added to reduce the effect of these characteristics by bridging cracks and holding the concrete together as fibres have a higher tensile strength (Naaman, 1987). A typical response and some characteristics of a concrete with entrained fibres is shown in Figure 2(a).

When fibres are added, the tensile response can change in a number of ways. Up to the initial cracking stress in Stage 1 of Figure 2(a), behaviour of the fibrous concrete is similar to plain concrete in that behaviour is relatively linear and the strain that takes place occurs in the concrete. As concrete is very stiff, displacements are very small and not significant enough to activate any fibre response so they have little effect in this region. After the cracking stress has been reached, Stage 2 can vary greatly. The maximum post-cracking stress can be altered depending on fibre type and volume used and may even be higher than the initial cracking stress for some specialist mixes (Naaman, 1987). However, it is shown as lower in Figure 2(a) as this is more representative of a standard mix with fibres included. Until the maximum post-cracking stress in this response curve, behaviour has been defined mostly by micro-cracking of the concrete. These cracks have now propagated significantly by this point so the load the concrete can carry has decreased considerably. Therefore, the fibre behaviour controls from now on and fibre failure and pull-out become the dominant failure modes. This results in a much more ductile tensile response as the concrete unloads and matrix behaviour tends towards fibre behaviour (Naaman, 1987).

In permeable concrete specifically, Rhedar et al (2014) finds that compressive properties are generally not affected by the presence of fibres favourably but that, in some cases, fibres clumping together affects the contact between aggregates and ultimately decreases compressive strength.

In tension, the fibres still act as in conventional concrete by bridging cracks and reducing macroscopic fractures, allowing some strength to be retained after cracking. Figure 2(b) shows two samples with porosities (ϕ) of 19% and 25%. For both samples, it is shown that adding a 1%

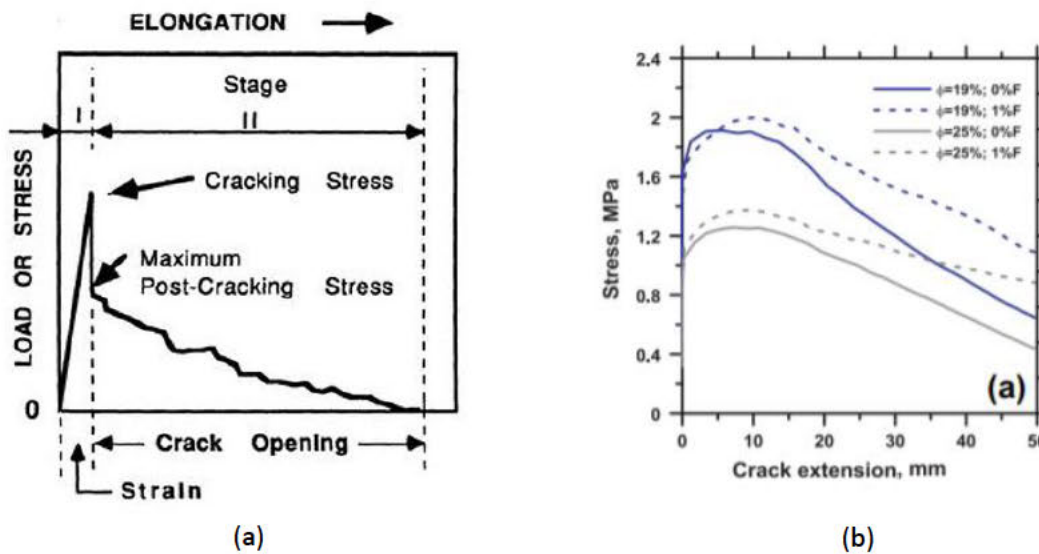


Figure 2: (a) A typical stress vs strain curve of high strength Fibre Reinforced Concrete in tension from Naaman (1987) and (b) experimental results of fibre effects on crack width elongation from Rhedar et al (2014)

volume of fibres (1%F) allows for more stress to be carried in the fibrous concrete at the same crack extension. As the responses for the fibrous mixes deviate from the plain mixes and converge, this shows fibre behaviour become more prominent as the crack width increases, as with normal concrete. Rhedar et al (2014) also states that adding fibres can increase the strain at which the “Maximum Post-Cracking Stress” described in Figure 2(a) occurs. The more fibres that are added, the more ductile the response, especially in the post-peak range.

2.2 Testing of Concrete Properties

Uniaxial tension in concrete is difficult to set up and measure. Therefore, a popular method for indirectly predicting tensile strength is a tensile splitting test as shown in Figure 3(a). A cylindrical specimen is loaded at a specifically calculated loading rate for the given dimensions until tension failure occurs (BSI, 2009). Schlaich and Schäfer (1991) explains that, when subjected to compressive loading from a thin source and positioned on a thin support, the compressive forces in the material spread out as shown in Figure 3(b). Due to the curve in the stress paths, significant transverse tensile strains are produced and lead to a splitting failure directly down the middle of the specimen where tensile stresses are strongest.

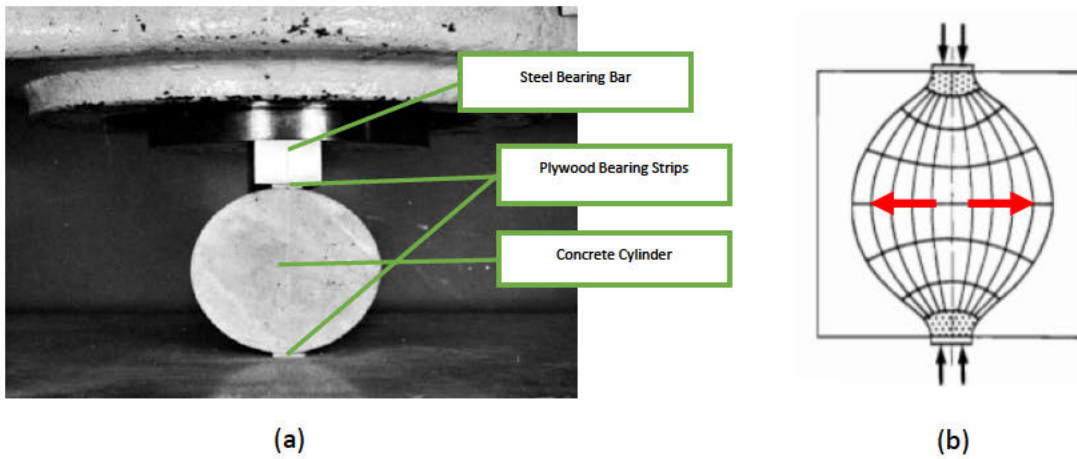


Figure 3: (a) Tensile splitting test demonstration adapted from ASTM (2017) and (b) stress path in compression adapted from Schlaich and Schäfer (1991)

The test does not involve direct measurement of tensile stresses however the load that is applied to the specimen can be used to determine the tensile stresses within the cylinder. The conversion of peak compressive loading to tensile splitting strength is through the BSI standard formula:

$$f_{t,sp} = \frac{2F_{max}}{\pi LD} \quad (1)$$

where $f_{t,sp}$ is the splitting test tensile strength, F_{max} is the peak load applied to the specimen, L is the specimen length and D is the specimen diameter.

The response of concrete during failure can be sensitive to size effects and method of obtaining the sample. Malárics & Müller (2010) has found that ratios between uniaxial tensile strength and splitting test tensile strength change depending the size of the sample and whether it was moulded or cored from an existing slab. Therefore, it is suggested that a conversion formula is used to estimate the uniaxial tensile strength. The conversion formula is given in CEB-FIP (2010) as:

$$f_t = \alpha_{sp} f_{t,sp} \quad (2)$$

where f_t is the uniaxial tensile strength, α_{sp} is the conversion factor between uniaxial tensile strength and splitting test tensile strength and $f_{t,sp}$ is the splitting test tensile strength.

Conversion factors vary between national standards however CEB-FIP (2010) recommends a value of $\alpha_{sp} = 1.0$ even though this value does not always represent the actual relationship. Table 1 from Malárics & Müller (2010) shows various relationships found experimentally between the uniaxial tensile strength and splitting test tensile strength. Specimens noted as cylinders have been moulded specifically whereas cores have been drilled from existing slabs of concrete.

In particular, the relationships for the cylinders are interesting as the additional power of $f_{t,sp}$ indicates that the relationship is not linear, as would be indicated by CEB-FIP (2010).

Table 1: Relationships between uniaxial tensile strength and splitting test tensile strength from Malárics & Müller (2010)

specimen property	D/L [mm/mm]	concrete aggregate	conversion formula
cylinder	150/300	gravel	$f_t = 1.46 \cdot f_{t,sp}^{0.77}$
core	150/300	gravel	$f_t = 1.14 \cdot f_{t,sp}$
core	75/150	gravel	$f_t = 0.90 \cdot f_{t,sp}$
cylinder	150/300	crushed	$f_t = 1.71 \cdot f_{t,sp}^{0.73}$

Investigations by Rocco et al (1997) also revealed the effects of changing the bearing plate size and sample size on the post-cracking response. Smaller samples and wider bearing strips lead to increased load measurements to the point where the post-peak recorded load was higher than the original cracking load. This provides the reasoning behind the standardisation of the test by national institutions such as the British Standards. Constant specimen sizes and bearing strip width of 15 mm are used in every test to reduce the potential size effects and provide comparable results.

2.3 Modelling of Concrete Behaviour

The modelling of concrete behaviour is based on non-linear finite element methods where a geometric model is discretised into small basic elements. These are then analysed, computationally or numerically, to determine parameters such as displacements, forces and accelerations at the nodes of each element to build up an approximate material response. Each node responds to the element loading situation according to a constitutive material model that governs the general material response over a single element. In the case of concrete, this material model is significantly non-linear. The total system of response equations from every element is then assembled and solved either implicitly or explicitly (Reddy, 2015). Implicit solving is defined by Sun et al (1999) as a process based on iteratively balancing forces through a Newton iteration scheme. Explicit methods involve integration of element mass and stiffness properties and finding displacements corresponding to discretised loading on each node.

Different types of constitutive model have been proposed for modelling the response and failure of concrete. Generally, these fall into one of the three main classes as plasticity, damage or damage-plasticity which is a combination of the previous two (Grassl et al, 2013).

Plasticity models that have been developed can be used to describe deformation in triaxial stress states such as confined compression. Menetrey and Willam (1995) describes the concept of a failure surface using three stress invariants with a deviatoric section that is nearly circular at high confinements but becomes more triangular at lower confinements. The significance of this failure

surface is that it can be developed further into linear-elastic and work-hardening theory where behaviour is described as linear-elastic inside this stress region but beyond this, further yield surfaces develop with plastic deformation or cracking occurring (Chen, 2007). Plasticity methods work well with triaxial stresses and deformation is generally well predicted but any stiffness decrease or softening that would be observed when a sample unloads due to damage in the material is not captured.

Damage models explicitly account for the reduction of stiffness and strength and are particularly effective in tension or unconfined compression. Damage was originally introduced as an approach by Kachanov (1958) which discusses the reasoning behind the change in behaviour of certain materials towards more brittle responses over time due to creep damage. The concept of microcracking in the material was developed and how this can reduce the stiffness as well as cause failure from fatigue at smaller strains than would be expected. Carol et al (1999) summarises many different perspectives on damage formulation. Isotropic damage is described as the simplest approach with a consistent stiffness reduction in all directions based on the level of damage incurred. More complicated approaches for anisotropic damage models may involve damage vectors or the more commonly used damage tensors. The general idea is that the reduction in stiffness and strength can be captured and the current stress-state can be determined precisely. A downside is that permanent deformations are usually not accurately described.

The combination of these models allows for a universal description in one complete model of failure in both tension and compression. This has led to the development of Damage-plasticity models. They allow the characteristics of permanent deformations and changes in material behaviour due to damage to be expressed together. Different approaches can be taken to this such as the energy-based approach of Ju (1989) which utilises the “damage energy release rate” to describe the energy needed for microcrack development based on stress invariants. Another model using stress invariants is CDPM2 (Grassl et al, 2013). This model is based on the effective stress principle for the plasticity part with damage formulated in terms of the strain encountered. The operation and implementation of this will be described in more depth in section 4.3.1.

Microplane approaches are also available where constitutive laws are applied in various directions within a material matrix. Descriptions of inelastic behaviour on each plane are then superimposed to form a complete response characterisation. Bažant and Oh (1983) developed a model suitable for concrete by utilising the strains, rather than stresses, between microplanes which form the matrix space and contact layers between nearby aggregate particles. This approach has the advantage that concentrated stresses caused by closely spaced aggregate particles do not invalidate the method. In the stress-based approach, stresses are assumed to be uniform across the material and resolved which is not necessarily an accurate description of the material state. A similar more recent example from Lian et al (2011) explains a discrete modelling technique for

pervious concrete where the forces associated with the cement paste bond, contact and friction between particles are calculated individually for a previously simulated mesoscale mesh.

2.4 Verification and Validation

This project involves the creation of a model of the tensile splitting test and it is therefore important to ensure that it is operating correctly and producing reliable and acceptable results. This means it must be verified and validated.

When simulating a physical experiment, a complete, accurate model of the specified test must consider all the relevant theory, dimensions, programming language and testing conditions to allow the model to perform to a predetermined standard. According to Babuska et al (2004), this is an iterative process that involves testing and refining the model towards its final representative state.

Verification is defined generally by Babuska et al (2004) as establishing that the operation of the model in relation to the programming code and theory is accurate and that all test conditions have been recognised as part of the model.

The two main types of verification are Code and Solution Verification. Code verification generally involves the running of simple test problems to find and solve any issues with the code that may affect the final simulations. These problems always have known analytical solutions that the model can be checked against. Solution verification involves estimating the uncertainties in the outputs of the model and comparing them against predetermined tolerances. This helps determine whether a sufficient level of verification, or confidence in the model output, is achieved. In this project, verification could be achieved by checking that the model response converges towards an expected solution or that overall behaviour is not radically dependent on the mesh size. As the analysis performed will be an explicit dynamic analysis, the response of changing the simulated time can also be studied to ensure results are not being distorted grossly by dynamic loading effects.

Validation is defined generally by Babuska et al (2004) as investigating whether relevant results produced by the model are accurate to a specified degree for the proposed use of the model and sufficiently represent the physical experiment. The results of the physical experiment must also be repeatable otherwise validation is impossible.

Verification and validation are both relative terms as both relate to a certain level of accuracy within tolerances based on the recognition that the model will not be completely and exactly valid. If the model under rigorous testing manages to meet these targets, then it will be judged to be sufficiently valid for use.

3 Physical Experiments

While parameters for concrete response may be gathered from literature, very few contain full stress vs strain/displacement response curves for compression and tensile splitting tests.

Combining results from different tests under varying conditions, curing processes and machines does not give confidence that the results will be consistent. Therefore, it was decided that concrete samples would be made and tested at the University of Glasgow, allowing for better comparisons to be made from comparable conditions.

3.1 Specimen Size and Number

Standard specimen sizes from concrete compression and tensile splitting tests are included in BS EN 12390-1:2012. A range of sizes can be chosen to use for the compression test, including both cubes and cylinders, however a 100x100x100 mm cube, shown in Figure 4(a), was selected due to availability of moulds. For the tensile splitting test, the length of the cylinder should be twice the diameter as stated in BS EN 12390-6:2009. The reference size is stated as a cylinder of 150 mm diameter and 300 mm length and so this was the size used in the experiments, as shown in Figure 4(b). 3 cubes and 6 cylinders were moulded for each concrete mix for use in both the mechanical and permeability experiments.

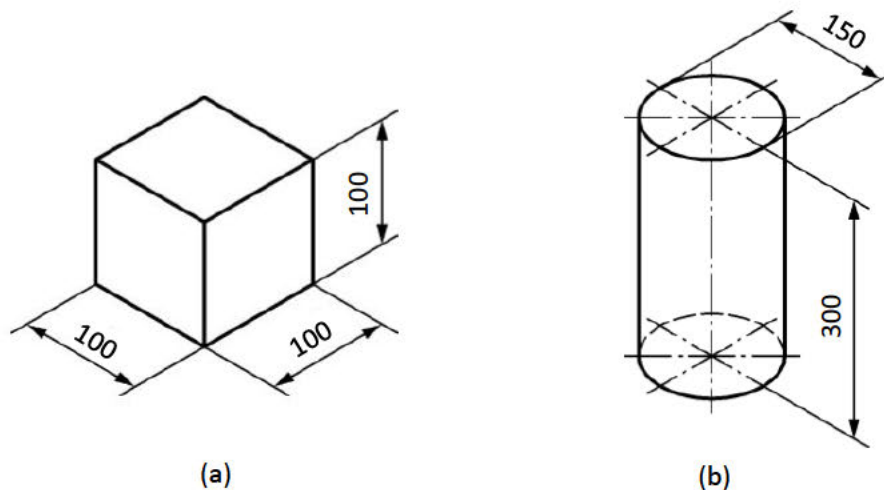


Figure 4: Sample geometry for (a) the compression test and (b) the tensile splitting test from BSI (2012)

3.2 Concrete Mix Design

For measurement of the effect of various constituents and combinations, 4 different mix designs were created as shown in Table 2. Each mix had a different combination of aggregate and steel fibre content so the effects of each constituent could be evaluated. The aggregates used were 20-

10 mm and 10-5 mm aggregates and assumptions were made about the density as these values were unknown (for simplicity, these will be referred to as 20 mm aggregates and 10 mm aggregates respectively from now on). The fibre type used was Bekaert Dramix® 65/35 BG which means that the fibres are 35 mm long and have an aspect ratio of 65 (Bekaert, 2018). The target void ratio was between 15% and 25% to agree with the usual range as stated in section 2.1.1 however it was understood this could vary when estimating constituent properties. The aggregate-to-cement ratio was also chosen as a standard value of 4.2 with 4 to 4.5 being commonly applied (Tennis et al, 2004) and a water to cement ratio of 0.3 employed. Full calculations for the mix designs can be found in Appendix A.

Table 2: Summary of constituents from mix design

Mix	Total Volume Mixed (m ³)	20 mm Aggregate (kg)	10 mm Aggregate (kg)	Cement (kg)	Water (kg)	Steel Fibres (kg)
Set 1	0.04073	63		15	3.9*	-
Set 2	0.04073	-	65	15.5	3.8*	-
Set 3	0.04073	63		15	4.5	1.6
Set 4	0.04073	-	65	15.5	4.6	1.6

* The calculated water was more than this value and can be found in Appendix A however, upon visual inspection, it was decided that these water levels were producing the desired moulding response

3.3 Sample Preparation

3.3.1 Mixing and Compacting

In preparation for the concrete placement, the cube and cylinder moulds were cleaned and then covered in oil to ensure that the concrete would not stick to them when stripped.

Wet permeable concrete behaviour should consist of being able to mould the concrete into a shape and then remain in that shape without falling apart or having cement paste dripping out of the specimen (Tennis et al, 2004). Therefore, in mixing the concrete, the aggregates and cement were mixed first (with fibres if included in mix) with water added in instalments so that the state of the concrete could be checked at regular intervals. Given that the added aggregates were not saturated surface dry before use, less water was used than originally calculated in the two plain mixes to gain the correct wet properties as described. This has been noted in Table 2.

Tennis et al (2004) states that vibration of permeable concrete for compaction can cause over-compaction and the permeability being affected as a result of void closure. To negate this risk, compaction was achieved with a tamping rod. As permeable concrete is not a complete matrix, the standard 25 hits was not observed and significant openings in the structure were still present at this point. Therefore, 30-40 hits was followed to ensure that the concrete would not prematurely fail due to overly poor compaction and presence of significantly large voids.

After stripping the specimens, their final weights were measured so that their actual densities could be assessed and to determine any discrepancies in the constituent calculations. Target densities and recorded densities are given in Table 3.

Table 3: Target and Recorded Densities from mix design and moulding

Mix	Target Density (kg/m ³)	Recorded Density (kg/m ³)
Set 1	2030	1856
Set 2	2095	1910
Set 3	2069	1896
Set 4	2134	1956

There are some noticeable discrepancies in the densities recorded in Table 3 as all of them are 150-200 kg/m³ lighter than calculated. It should be noted that the mix design calculations were not detailed, as implied in section 3.2. In particular, the density of the aggregate was estimated as just its own density. No estimation was made of how much may stick together in sub-optimal positions within the concrete matrix when not highly compacted. This is most likely the cause of the lighter recordings since the cement, water and fibres should be able to fit between the gaps created by the aggregates relatively evenly. It should be noted however, that the comparative weights between samples are consistent with the calculated densities, so this gives some confidence that the mixing and compacting procedure has been effective at producing consistent mixes.

3.3.2 Curing, Permeability Testing and Final Preparation

After stripping and weighing, the concrete was placed in water for curing.

After 45 days, it was necessary to take the samples out so that porosity and permeability testing could be performed before the fracture testing to give a larger sample size for this component of the investigation. This involved placing them in an oven at 40 degrees Celsius to dry out completely and then have water passed through them multiple times to ensure consistent measurements could be justified for each sample.

After the permeability testing was completed, the samples were dried out fully again. The cylinders also were painted white on one end so that crack opening in the splitting test could be more easily observed.

The total time between the mixing and testing was 55 or 56 days as the first set of samples was tested over 2 days.

3.4 Concrete Testing

3.4.1 Compression Test

3.4.1.1 Setup

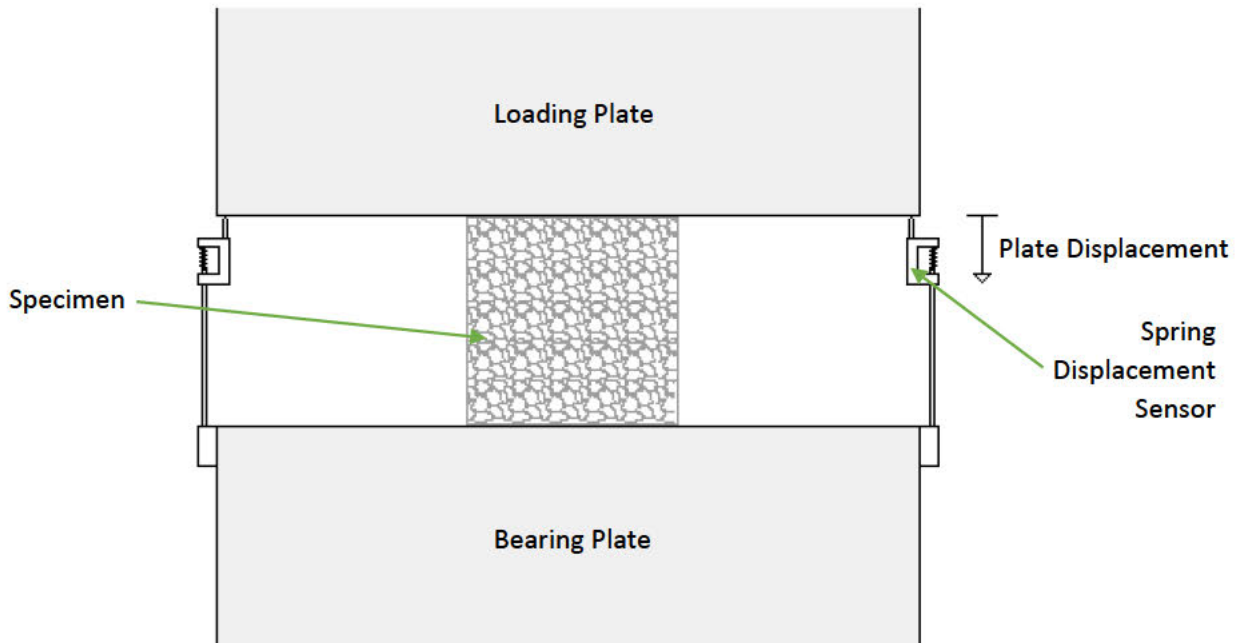


Figure 5: Compression test setup

The compression test was completed as a standard compression test generally under conditions of BS EN 12390-3: 2009 but with displacement control. The setup is shown in Figure 5. As a trial, the first sample was fractured at a plate displacement loading rate of 0.1 mm/min. However, since many samples had to be tested and the first test took a long time, it was decided that 0.2 mm/min would be used thereafter. These rates are relatively similar to previous tests completed in literature.

The failure curve was recorded by sampling the measured reaction load on the base plate in increments of loading plate displacement. For the first test, the load was taken every 0.025 mm and, in the other tests, every 0.05 mm. The maximum failure load and the corresponding displacement were also noted. The test continued until it was decided that a sufficient amount of the observable post-peak behaviour had been recorded.

Initially, the compressive load recorded was plotted against the loading plate displacement for comparison and discussion between samples.

For the extraction of model parameters for the homogeneous mesh in section 5.1.4, the average stress and strain had to be considered.

The main load results were converted into an average compressive stress through the standard stress formula:

$$\sigma_c = \frac{F_c}{A_b} \quad (3)$$

where σ_c is the compressive stress, F_c is the compressive force (reaction from the bearing plate) and A_b is the area of the faces of the cube. This approach assumes that all stresses are the same across the entire specimen even though the complex material structure means this will not be the case.

The average compressive stress was then plotted against the average strain, ε_{ave} , induced on the sample. The average strain is calculated using the length of the sides of the cube samples, L_{cube} , and the displacement of the loading plates, ΔL_{plate} , in the formula:

$$\varepsilon_{ave} = \frac{\Delta L_{plate}}{L_{cube}} \quad (4)$$

The average strain is used as any strains calculated in this manner may not represent the true strains occurring within the material, again due to its strongly inhomogeneous nature.

3.4.1.2 Compression Test Results

Table 4 summarises the maximum loads observed in the compressive test. These have also been converted into the compressive strengths using formula (3) above. Figures 6 and 7 show the compression load failure curve for all samples against the loading plate displacement. The curves have been arranged so that the plain concrete samples are paired with their fibrous counterparts according to aggregate size. The inclusion of the fibres is the more important alteration of the constituents and this allows the influence of them on the mechanical performance to be clearly visible.

Table 4: Summary of Maximum Compressive Loading Results

Set Number	Type	Average Maximum Load (kN)	Average Compressive Strength (MPa)
1	Plain 20 mm	85.3	8.53
2	Plain 10 mm	188.2	18.82
3	Fibrous 20 mm	150.3	15.03
4	Fibrous 10 mm	267.8	26.78

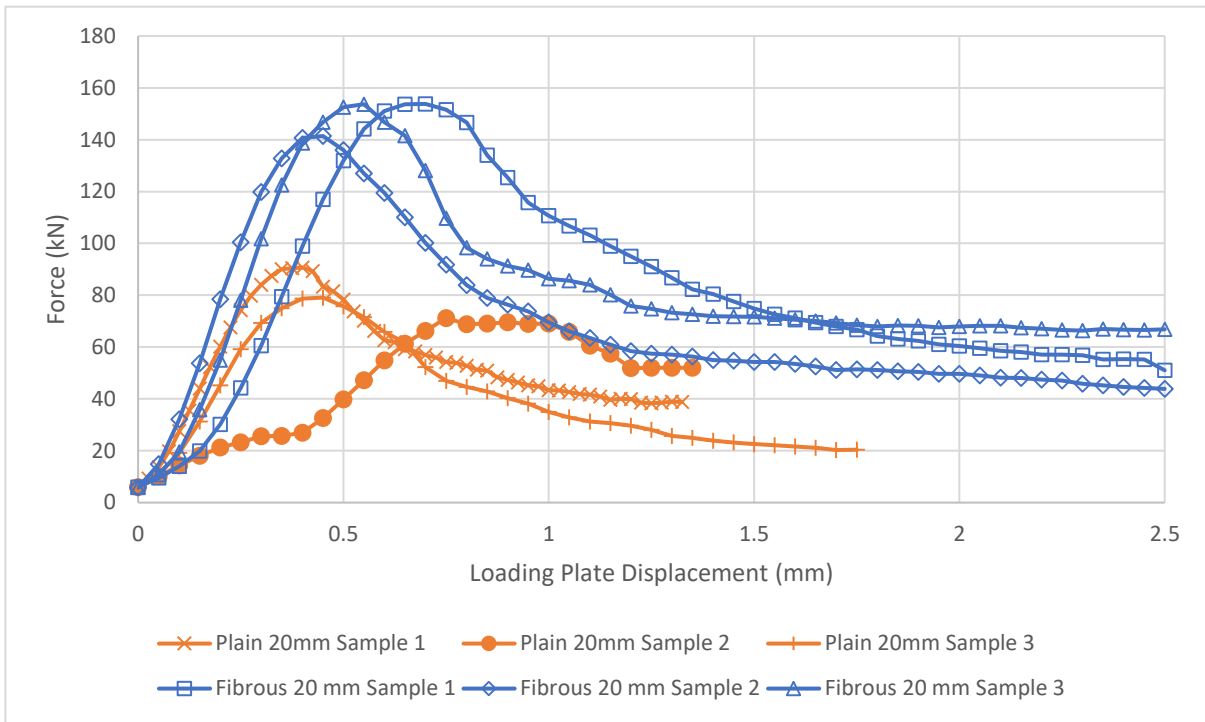


Figure 6: 20 mm Aggregate Compressive Force vs Load Displacement Comparison with and without Fibres

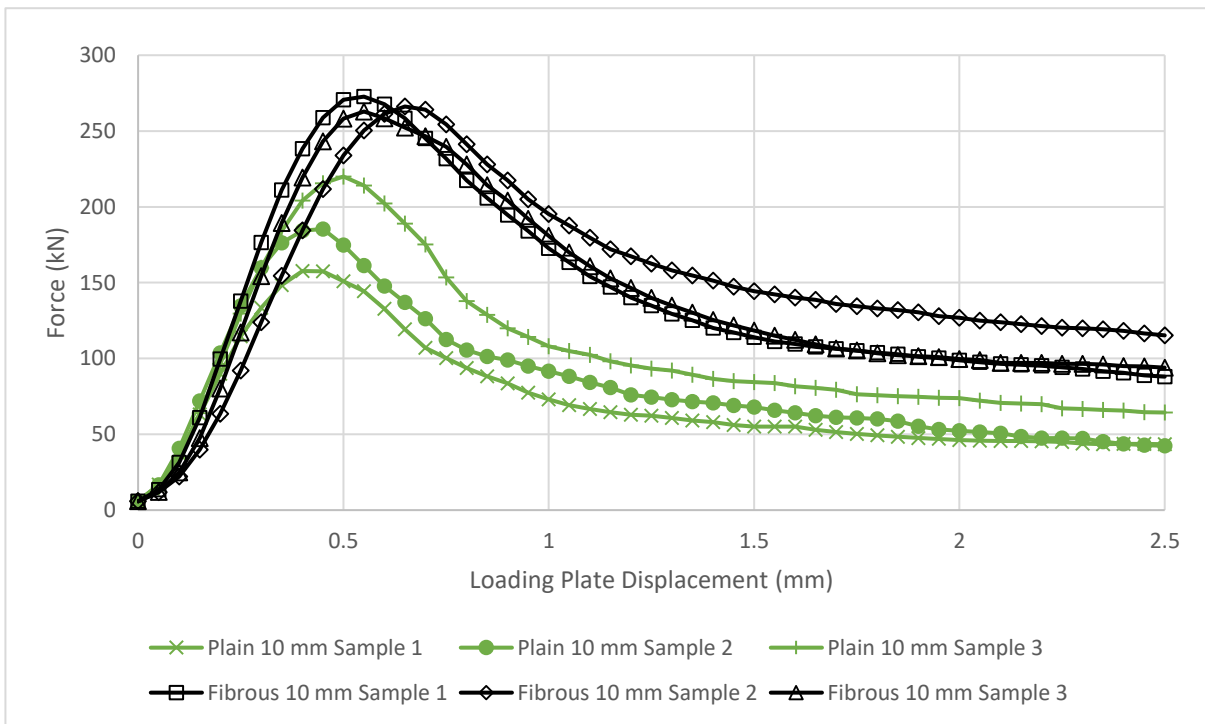


Figure 7: 10 mm Aggregate Compressive Force vs Load Displacement Comparison with and without Fibres

3.4.1.3 Discussion

As mentioned in section 2.1.2, previous studies found that the compressive properties for porous concrete were not hugely affected by the addition of fibres but from Figure 6, discounting the clearly outlying measurements of plain sample 2 (this result is discounted from all following analysis), the strengthening effects of the fibres can clearly be seen in this experiment, contradicting the earlier investigations. The average failure load of the plain 20 mm aggregate samples was around 85 kN and this corresponds to an average compressive stress of 8.5 MPa. For the fibrous samples, this value rises significantly to around 150 kN or 15 MPa in compressive stress which is an increase of just over 76%. This is surprising that the strength would be affected so greatly however the gain is consistently replicated in each of the fibrous samples. Since the samples were stored and tested in approximately the same manner, the consistency of the load carried by the fibrous samples gives some confidence that the experimental method was reliable and so the strength gain must be due to the actual material response.

The gradient of the curves in Figure 6, although not directly depicting strain, can also be linked to the bulk stiffness of the material. The slightly steeper loading response seen in the fibrous samples indicates that the overall bulk stiffness is marginally higher than the plain samples although the difference is not as significant as the difference in strength. This leads to higher plate displacements recorded at failure with an average value of around 0.55 mm (after accounting for the significant underdeveloped contact time at the beginning of fibrous sample 1 as well) compared to around 0.4 mm for the plain samples. This indicates a more ductile pre-failure response can be obtained with fibre inclusion for this particular aggregate size.

The 10 mm aggregate samples also show an improvement in mechanical properties as shown in Figure 7. This time however, the strength increase is clearly not as dramatic in terms of relative improvement. The fibrous samples reached around 268 kN or 26.8 MPa while the plain samples reached around 188 kN or 18.8 MPa which is an increase of only 44%. This may, in part, be due to the coarse material having a more irregular structure so allowing fibres to bridge the irregularities together will have more effect than doing the same in a more homogeneous material such as the 10 mm samples. Furthermore, the loads recorded in the fibrous samples are not dissimilar to strengths that could be recorded in conventional concrete cubes.

A point to note is that a parallel compression study for conventional concrete, produced at the same time with this method performed by Middlemiss (2019), found a significant decrease in compressive strength when fibres were added. The compressive strength for the plain concrete was found as 42.6 MPa but adding 0.5% volume of fibres decreased this to 25.8 MPa. Adding 1% volume of fibres lowered it further to 22.8 MPa which is lower than the 10 mm permeable samples. This shows that care must be taken to ensure the fibres are actually benefitting the specified mix in its intended purpose.

The bulk stiffness is again slightly higher for the fibrous samples but not significantly and as before, this leads to higher plate displacements failure with very similar values to the 20 mm samples recorded for both plain and fibrous samples.

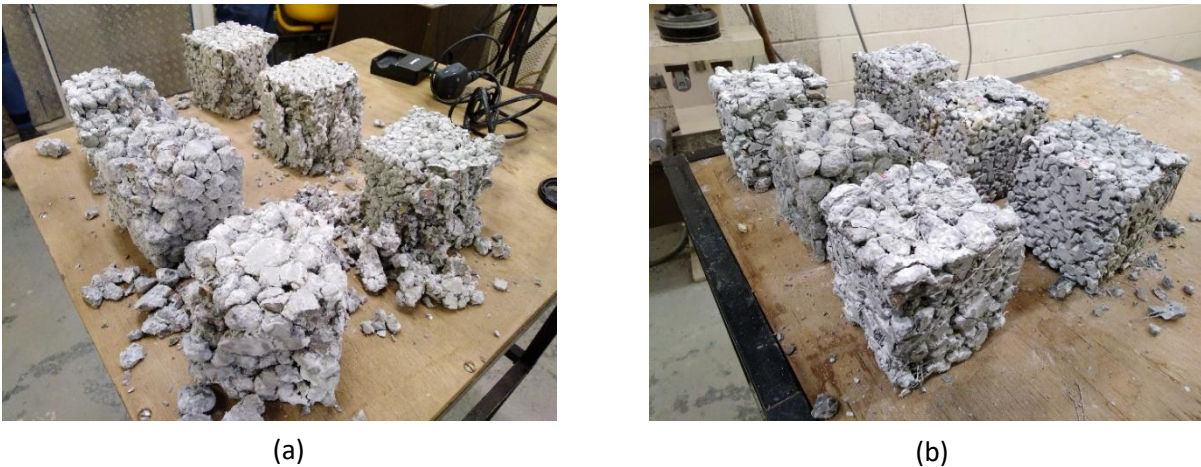


Figure 8: (a) Crumbling of plain concrete samples and (b) integrity of fibrous samples

What can be seen from both samples is the rise in load capacity in the post-peak regime. The load capacity falls slowly but steadily in all samples as the loading plate displacement increases but the fibrous samples are at a consistently higher load. Figure 8 may show the reason for this as the fibrous samples in Figure 8(b) stay together much better than the plain samples in Figure 8(a) which have completely cracked and fallen apart. The added resilience to cracking is also consistent the mechanism for the significant increase in strength. Cracks that open are bridged with the fibres and halted from propagating so the energy required to open and join cracks is significantly increased. Therefore, the energy provided by the loading must be higher to cause cracking failure.

Rather surprisingly, a significant amount of plastic deformation is visible in all samples before failure which again, contradicts earlier investigations. The peak of each curve is rounded and not demonstrating any sudden transition from loading to softening which is more in line with conventional concrete behaviour. However, since this is a consistent result and the curve appears very similar in most samples, propagation of microcracks is likely the governing overall failure mechanism rather than any premature collapse due to weak planes in the material.

A final feature of every response to note is that there is a strong upwards curve at the beginning of the each test. This is mostly due to the undulating nature of the surface meaning contact with the loading plate is not entirely developed until some minor displacement takes place.

3.4.2 Tensile Splitting Test

3.4.2.1 Setup

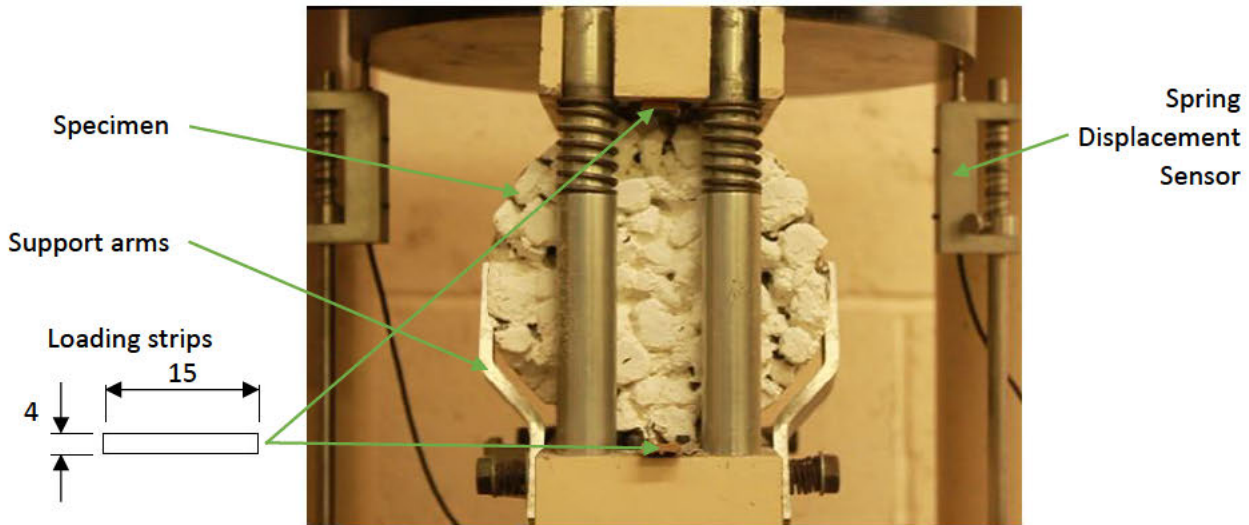


Figure 9: Tensile Test Loading Strip Geometry and Setup

The tensile splitting test was also completed in a standard manner according to BS EN 12390-6:2009. The setup is shown in Figure 9. The only differences being that the ends of the specimen were uncovered so the crack propagation could be observed with a camera and all tests were done with a set bearing bar displacement rate of 0.2 mm/min for comparability.

The failure curve was observed in the same way as the compressive tests with the same increments of 0.05 mm and with the maximum load and displacement noted. For all but one of the tests, the cylinder did not split dramatically enough to trigger the machine to cut-off so these tests also recorded post-peak behaviour. Again, the reaction load was plotted against the loading plate displacement as strain does not bear any physical meaning for this test. The strains required to crack the material are barely visible and failure is localised so any measured “strain” between two points each side of the crack is not the actual strain occurring in the middle. Also, any post-peak loading behaviour recorded is dependent on the mode of failure and the position of the crack itself since the ability to see a crack in this test likely means the concrete matrix already has no stress capacity. Therefore, it is only recorded for comparative purposes and bears no relation to tensile fracture energy or post-peak ductility.

The maximum load was converted into the approximate maximum tensile splitting stress, $f_{t,sp}$, using the previously stated formula (1):

$$f_{t,sp} = \frac{2F_{max}}{\pi LD} \quad (1)$$

This splitting tensile strength should not necessarily be taken as the uniaxial tensile strength as found by Malárics & Müller (2010) so the strengths determined here are specifically defined as such. A method for calculating an approximate conversion factor, α_{sp} , to determine the uniaxial tensile stress, f_t , is given in section 5.1.1.

The camera was set-up so that any observable crack propagation and widening could be analysed give an indication of the tensile crack opening mechanism during the splitting test.

3.4.2.2 Results

Table 5: Summary of Maximum Tensile Loading Results

Set Number	Type	Average Maximum Load (kN)	Average Splitting Tensile Strength (MPa)
1	Plain 20 mm	80.6	1.14
2	Plain 10 mm	99.7	1.41
3	Fibrous 20 mm	94.7	1.34
4	Fibrous 10 mm	135.7	1.92

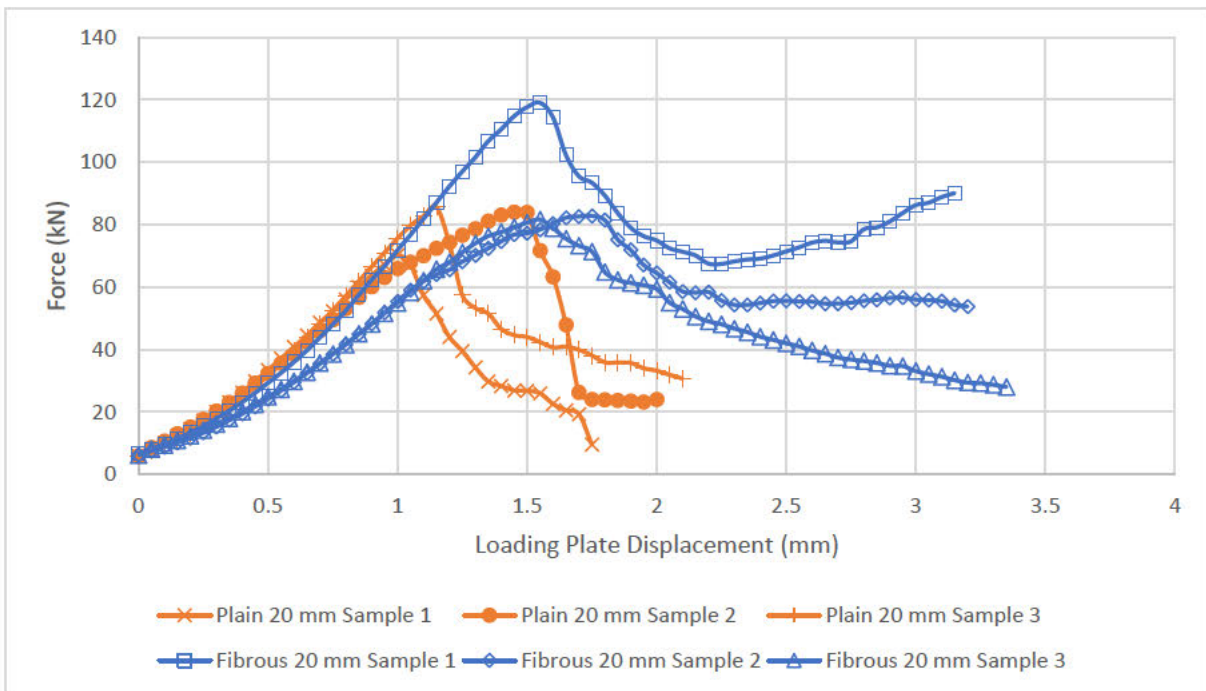


Figure 10: 20 mm Aggregate Force vs Load Displacement Comparison with and without Fibres

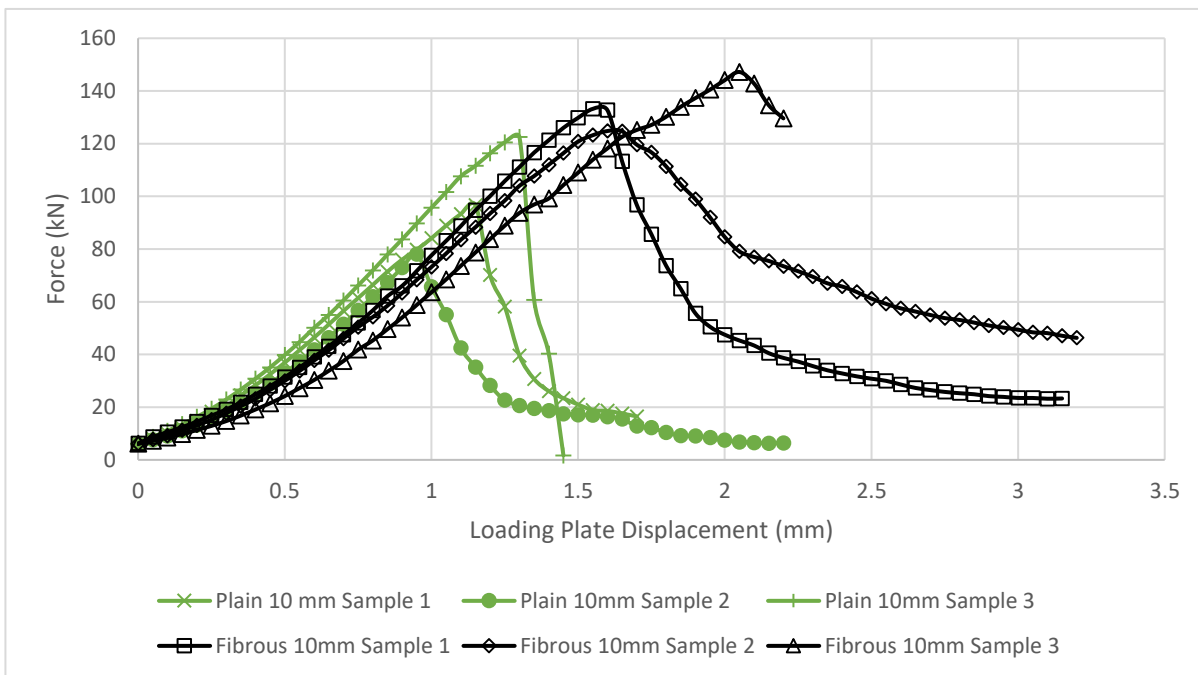


Figure 11: 10 mm Aggregate Force vs Load Displacement Comparison with and without Fibres

3.4.2.3 Discussion

As with the compression tests, the addition of fibres leads to improvement in the mechanical properties under tensile load but interestingly, to a generally lesser degree.

The plain 20 mm samples in Figure 10 failed on average at a load of 80 kN which corresponds to an $f_{t,sp}$ value of 1.14 MPa whereas the 20 mm fibrous samples failed on average at 95 kN or an $f_{t,sp}$ value of 1.34 MPa. This is an increase of 17.5%. The average of the fibrous samples is skewed by sample 1 which reaches nearly 120 kN compared to loads of 80 kN for the other two. However, this also seems to be the sample that follows the original plain sample loading gradient as the other samples deviate on a less stiff response curve so it has still been retained in the results.

Theoretically, sample 1 follows the expected curve with crack propagation limited by the presence of fibres so loading should be able to rise higher. The other samples failing at loads lower than the highest plain samples may be caused by the unpredictable distribution of fibres across areas of highest stress and whether cracks can negotiate their way around the fibres following the weakest route. In the first fibrous sample, it seems likely that the fibres were well distributed and cracks could not propagate easily but the other two samples did not have an efficient or effective fibre distribution.

What is still clear in the 20 mm aggregate samples is that the initial apparent softening response is significantly lessened. The plain samples drop away very quickly to low levels after failure and at lower displacements. The fibrous samples are held together by the fibres slowing crack propagation and do not split in half as quickly.

The 10 mm aggregate samples in Figure 11 show a similar trend however the spread of the plain sample maximum loads is considerably greater while the fibrous samples show much more consistent loading. The inclusion of fibres in the 10 mm aggregate samples increases the average failure load to 135 kN or 1.92 MPa, compared to an original average of 100 kN or 1.41 MPa. This is an increase of 36%. The plate displacement at failure is also increased and as with the 20 mm samples, the softening response is not as extreme. The more consistent fibrous sample strength means that a greater relative strength improvement is shown when compared to the 20 mm samples. Further samples would be required for both the 10 and 20 mm aggregates to determine whether these results are regular or whether they can be attributed to statistical outliers.

Additional post-peak behaviour after the initial cracking softening is sporadic but does show some general trends based on how the samples stay together. The load capacity in all samples of the plain materials drops to generally quite a low level and continues to fall since both fractured halves of the sample are able to freely move away from each other. This means that over time the loading area from the strip decreases however some load is still able to be carried through the compression of each half. The fibrous samples on the other hand generally remain at a much higher level since they are held together by the fibres. The first 20 mm fibrous sample begins reloading again even though the stress state of the concrete material has entirely changed. If displacement had continued further, this reloading may have been observable in other samples as well. The central tension in the cement and aggregates has disappeared however the sample is held together by the fibres utilising their tensile strength and bridging the major cracks. Since the sides are not pushed apart as easily, the specimen continues to be loaded by the plate as it would before fracture with aggregates interlocking. However, now the aggregates and cement are mainly in compression while the fibres are in tension. This situation is favourable for the respective materials and the load can now significantly before potentially fibre pull-out or compressive failure. This complex situation also means the tensile stress in the material cannot be estimated during this period as the cylindrical stress estimation, formula (1), is not appropriate.

This exposes the main issue with using the splitting test in this experiment. The tensile post-peak behaviour, where the fibres will generate the greatest benefits against tensile crack opening, is not truly represented and does not provide any useful insight into what effect they will have in pure tension. The only real information that indicates that the fibres are affecting the response is the change in splitting tensile strength, the difference in splitting test post-peak behaviour mentioned above and the immediate apparent softening response. Any further deductions on crack opening width, uniaxial tensile softening and estimations of fracture energy would require a different type of test to be undertaken.

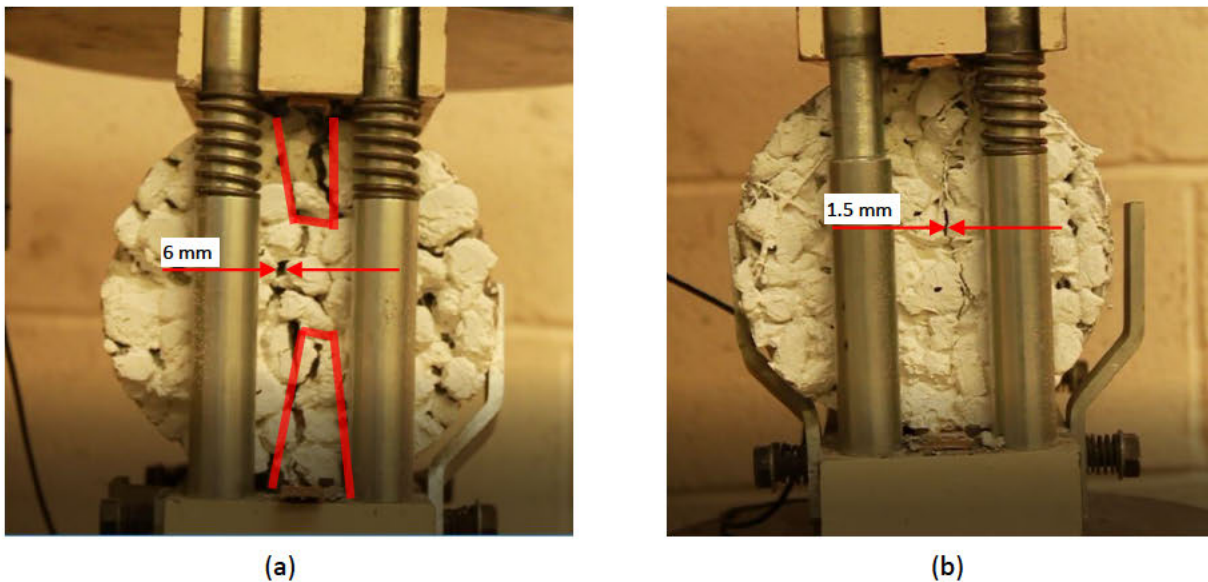


Figure 12: Crack opening behaviour for (a) sample 1 of the 20 mm aggregate plain mix with the wedge highlighted and (b) sample 3 of the 20 mm aggregate fibrous mix

Since the splitting test cannot measure tensile crack opening, the camera setup did allow some information about the crack-opening mechanisms taking place in the test after failure to be deduced. Rather than widening the crack through tensile stresses, the crack-opening of the plain materials appears to be due to the bearing strips driving a wedge of failed material underneath (or on top) into the sample and forcing it apart. This is shown by sample 1 of the plain 20 mm aggregate mix in Figure 12(a). This widened the crack width at the end of the test to over 6 mm. Conversely, this behaviour was much less prevalent in the fibrous samples. As an example, Figure 12(b) shows sample 3 of the fibrous 20 mm aggregate mix. The fibres help maintain the material integrity and reduce crack growth so at the end of the test, the crack width was reduced to around 1.5 mm even though plate displacement was nearly twice as large. This behaviour has also been observed for conventional concrete (Middlemiss, 2019). This type of behaviour will be useful for determining the overall accuracy of the simulation since it is likely the model will predict the main mechanism and shape of cracking failure but post-failure behaviour such as this may not be captured.

What should be noted in these results is the multiple different modes of failure recorded, particularly in the plain 20 mm aggregate samples. The 3 different samples after failure are shown in Figure 13. The first sample in Figure 13(a) shows complete failure as expected with a straight crack through the middle, the second in Figure 13(b) shows very slow development of a central crack while the third, in Figure 13(c), cracked diagonally in an abnormal failure. While this would be very rare in conventional concrete, it highlights the potential for weak planes within large aggregate permeable concretes. The 10 mm samples showed much more consistent central failure as shown in Figure 14(a).



(a)



(b)



(c)

Figure 13: Tensile Splitting Failure modes of the 20 mm plain concrete for (a) sample 1, (b) sample 2 and (c) sample 3

The fibrous samples, being held together by the fibres as mentioned, showed a significant reduction in crack width to the point that it was difficult to determine the exact mode of failure. However, some cracks were visible along the radial edges of the samples and cracks were not always through the centre suggesting that they were propagating along lines of weakness between the stabilising fibres. Some examples of this are shown in Figure 14(b). This is relevant to the final outcomes of this investigation as the fibres provide a back-up to cracking failure. The usage of permeable concrete in pavements and roads mean that this kind of failure could be quite likely at exposed edges so extra resistance to crumbling apart provided by fibres is useful.



(a)



(b)

Figure 14: Tensile Splitting Failure modes of (a) a plain 10 mm sample and (b) the 10 mm fibrous samples

4 Material Simulation Models

The compressive strength can be approximated directly from the results of the compression test assuming that stresses and strains are averaged through the material. On the other hand, the splitting test tensile strength may not be a good representation of the actual tensile strength without the determination of a conversion factor, as discussed in section 2.2. To formulate a potential conversion factor for permeable concrete, it was decided that the splitting test would be simulated as a finite element analysis. The analysis was further used to determine whether information about the behaviour, both pre-peak and post-peak, could be extracted from the splitting test simulation as this would determine the applicability of the CDPM2 model and mesh simplification method for future applications.

This section focusses on the description of material models and features of the LS-DYNA software. Section 5 discusses the actual simulations undertaken, specific model inputs and the results.

4.1 Modelling in Macroscale

In this investigation, the mesh will be simulated as a homogenous material with parameters of CDPM2 altered to reflect results gained from the permeable concrete experiments. This provides a much more flexible and general approach where the mesh does not need to be regenerated if the constituent properties are changed and, since the mesh is much simpler, computational time can be saved. This success of this method with CDPM2 will be analysed in the discussion of the results.

4.2 Non-Linear Finite Element Method

The solution method will consist of an explicit dynamic non-linear finite element simulation, as found in literature, that pairs well with homogeneous meshes. The nature of this solution method means that significant computation is required to solve large diagonal matrices over several time-steps dictated by the geometry of the discrete elements. Required features of the analysis such as the specific constitutive material models and time steps are described in greater detail below.

4.3 CDPM2 Non-linear Finite Element Constitutive Model

CDPM2 (Concrete Damage-Plasticity Model 2) is a damage-plasticity constitutive model that describes the failure of concrete by combining the effects of plasticity based on effective stresses with a damage model relating to occurring strain (Grassl et al, 2013).

4.3.1 Model Operation and Implementation

CDPM2 is a further refinement of CDPM1 developed by Grassl and Jirásek, (2006) that related well to physical experiments, however potential improvements that would allow for extensions of the model were noted. In the original model, only one damage parameter was utilised for both tension and compression and while for some circumstances, this was sufficient, for situations such as tensile failure transitioning into compressive failure, it could not capture the response realistically. Therefore, the refined model has one damage parameter for compression and one for tension. The basic stress-strain formula that forms the basis of the model is described in Grassl et al (2013) as:

$$\sigma = (1 - \omega_t)\bar{\sigma}_t + (1 - \omega_c)\bar{\sigma}_c \quad (5)$$

where $\bar{\sigma}_t$ is the positive part of effective stress tensor σ , $\bar{\sigma}_c$ is the negative part of effective stress tensor σ and ω_t, ω_c are scalar damage variables where a value of 0 corresponds to no damage and 1 corresponds to full damage.

It is based on the effective stress tensor as the model functioning on nominal stresses would be restricted to confined compression and strain hardening. The response uniqueness would not be satisfied and more than one solution could be obtained for certain strain histories in other load cases. These restrictions do not apply to the models based on effective stress and describe softening without divergence in solutions (Grassl et al, 2013).

The plasticity model is dependent on the yield function and the flow rule primarily. The Haigh-Westergaard co-ordinates based on volumetric effective stress, $\bar{\sigma}_v$, deviatoric effective stress norm, $\bar{\rho}$, and the load angle, $\bar{\theta}$, along with hardening variable, κ_p define the cylindrical shape of the yield surface. κ_p relates the plastic strain rate loading conditions to the model and determines the values of q_{h1} and q_{h2} which describe yield surface progression. A further function, $r(\cos \bar{\theta})$, determines the deviatoric section shape (Grassl et al, 2013).

In a general sense, the yield surface defines the limits of suitable stress states that can exist within the concrete before failure. It can be specifically represented as Haigh-Westergaard Co-ordinates within a 3D principle stress space which the CDPM2 model utilises. The 3 constituent Haigh-Westergaard Co-ordinates are described in Grassl (2018) as:

- The volumetric stress length

$$\xi = \sqrt{3}\bar{\sigma}_v \quad (6)$$

where $\bar{\sigma}_v$ is the volumetric stress.

- The deviatoric stress length

$$\bar{\rho} = \sqrt{2J_2} = \sqrt{\left(\frac{1}{3}\right)((\sigma_1 - \sigma_2)^2 + (\sigma_2 - \sigma_3)^2 + (\sigma_3 - \sigma_1)^2)} \quad (7)$$

where σ_1, σ_2 and σ_3 are principle stresses and J_2 is a stress invariant.

- The lode angle

$$\cos(3\bar{\theta}) = \left(\frac{3\sqrt{3}}{2}\right)\left(\frac{J_3}{J_2^{1.5}}\right) \quad (8)$$

where J_3 is a different stress invariant and is defined as $J_3 = \frac{1}{3}(s_1^3 + s_2^3 + s_3^3)$ where s_1, s_2 and s_3 are deviatoric stresses.

The representation of these coordinates is described in Figure 15.

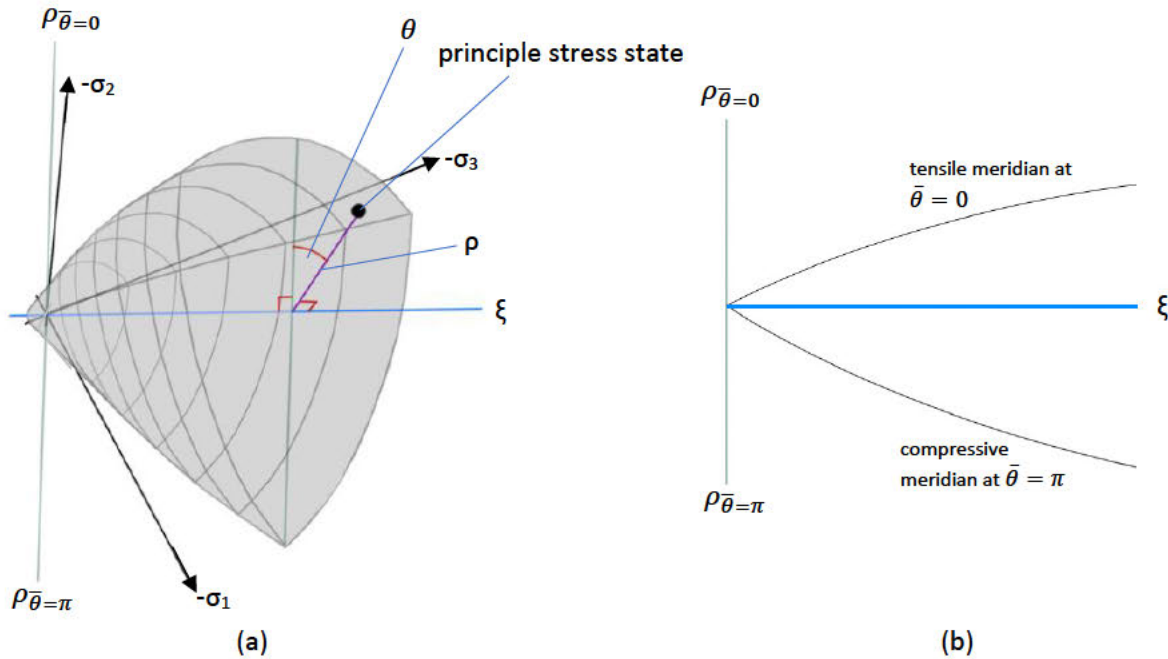


Figure 15: (a) Haigh-Westergaard Coordinates deviatoric section representation of the failure surface in a 3D principle stress space (adapted from Paliwal et al, 2017) and (b) compressive and tensile meridians

If a section along the ξ and $\rho_{\bar{\theta}=0}$ axes in Figure 15(a) is taken, the compressive and tensile meridians of the yield surface are revealed and are parabolic (Grassl and Jirásek, 2006) as in Figure 15(b). The deviatoric section and meridian appearances rely on the eccentricity parameter, **ECC**, which is given in Jirásek and Bažant (2002) as:

$$ECC = \frac{1 + \epsilon}{2 - \epsilon}, \quad \epsilon = \frac{f_t(f_{bc}^2 - f_c^2)}{f_{bc}(f_c^2 - f_t^2)}, \quad f_{bc} = 1.16f_c \quad (9)$$

where f_t is the concrete tensile strength (measured or estimated) and f_c is the measured concrete compressive strength. This means that the shape of the section will be different for changing ratios

of f_t and f_c . Also, for larger confining stresses in triaxial testing, the deviatoric section becomes more rounded and less triangular (Grassl and Jirásek, 2006). The CDPM2 model makes use of the parameter **ECC** when determining the stress-state in relation to the yield surface.

The flow rule used by the model is determined by deviatoric and volumetric elements from which the derivation of a dilation variable, m_g , can be achieved. This describes the ratio between volumetric and deviatoric parts of plastic flow and is based on the principles that strains in a transverse direction to the loading are produced in tension while in compression, volumetric expansion is detected. This flow rule is non-associated and so plastic flow is not restricted to a direction normal to the plastic potential and plastic strain rate is not related to the yield function.

The basis of the damage model is that a threshold of strain, ε_0 , must be reached for damage to initiate. For uniaxial tension, $\varepsilon_0 = \frac{f_t}{E_c}$, where E_c is the material Young's Modulus. Strains can be related to damage if the equivalent uniaxial strain, $\tilde{\varepsilon} = \frac{\sigma_t}{E_c}$, where σ_t is the uniaxial tensile stress, breaches ε_0 . In this case, f_t could be regarded as a one-dimensional strength envelope. In more complex stress regimes, this concept is used to predict damage when the yield surface is reached. Damage is represented in the form of damage variables ω_t and ω_c , which themselves are each described by a unique set of three history variables each for tension and compression. Four of the six variables depend on a ductility measure, x_s , that relates effects of complex stress states to the softening regime. A further parameter, α_c , is used to determine whether tensile or compressive damage is occurring based on the combination of principle stresses.

Grassl et al (2013) states that in tension, a bilinear softening law is used that relates the stress to the inelastic strain and is shown in Figure 16(a). ε_t denotes the inelastic strain in this case and is converted to a displacement by a variable, h , which is dependent on the mesh geometry specified. This ultimately represents the crack width. It has to be plotted this way as the failure is localised therefore measured displacements will not represent the strain in the material. In compression, the stress vs strain law used is exponential and this is shown in Figure 16(b). The variables f_t , f_{t1} , w_{f1} , w_f , A_s and ε_{fc} are material properties and thresholds for how softening behaviour is defined or where material response changes. They are further described in section 4.3.2.

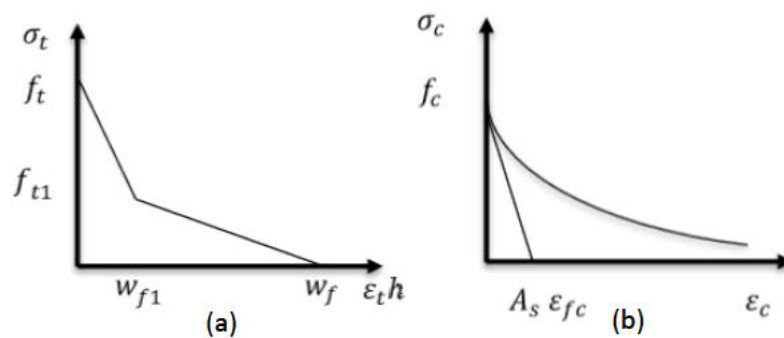


Figure 16: (a) Bilinear softening law used in tensile post-peak response and (b) exponential softening response used in the compressive post-peak regime from Grassl (2016)

CDPM2 is explicitly implemented where time is also segmented along with the model geometry. New results for each time step progressively build on the previous step stemming from integration of the fundamental constitutive equations and iteratively solving on a global level.

To solve the local stress situation, a form of predictor-corrector method is used. Trial principle effective stresses are determined at the start of each step from known displacements and are evaluated as inside or outside the yield surface in the Haigh-Westergaard co-ordinate space. The trial directions of these principle stresses can be also be predetermined and do not change throughout the step. If the yield surface is not reached, plasticity variables will not change during the step and the response will be fully elastic. This response is used as the first approximation in the scheme to calculate the two unknown stress invariants, $\bar{\sigma}_v$ and $\bar{\rho}$. The Lode angle is unchanged throughout the time step and the trial value can be used so it is not an unknown. Once the stress invariants are found, they are then used to evaluate the final effective stresses in the Haigh-Westergaard co-ordinate space to create the effective stress tensor that can be manipulated to determine other model characteristics. The next step is then initiated and the process is repeated until a specified end time.

4.3.2 LSDYNA Constitutive Model - MAT_CDPM

CDPM2 has specific input cards for use in LSDYNA, shown in Table 6, called by the command MAT_CDPM. An explanation of each of the input parameters is given, adapted from Grassl (2016). These parameters describe specific material properties such as strength and stiffness that generate unique responses of loaded samples. Individual values that will be changed with the introduction of the permeable concrete and fibrous models are highlighted in section 5.1.4.

Table 6: Input cards for MAT_CDPM in LSDYNA including default values from Grassl (2016)

Card 1	1	2	3	4	5	6	7	8
Variable	MID	RO	E	PR	ECC	QH0	FT	FC
Type	A8	F	F	F	F	F	F	F
Default	none	none	none	0.2	AUTO	0.3	none	none

Card 2	1	2	3	4	5	6	7	8
Variable	HP	AH	BH	CH	DH	AS	DF	FC0
Type	F	F	F	F	F	F	F	F
Default	0.5	0.08	0.003	2.0	1.0E-6	15.0	0.85	AUTO

Card 3	1	2	3	4	5	6	7	8
Variable	TYPE	BS	WF	WF1	FT1	STRFLG	FAILFLG	EFC
Type	F	F	F	F	F	F	F	F
Default	0.0	1.0	none	0.15*WF	0.3*FT	0.0	0.0	1.0E-4

MID - Material Identification Number unique to the material that can be chosen arbitrarily and does not affect material response.

RO - ρ_c : Concrete bulk density. Bright and Roberts (2010) states that the mean value of normal weight concrete is 24 kN/m³ or 2400 kg/m³. This is within the range of 2000 - 2600 kg/m³ as stated in CEB-FIP (2010) and so will be used for the validation analysis of the simulation. Densities of the permeable concrete mixes used in the experiments have already been calculated in section 3.3.1.

E - E_c : Concrete Young's Modulus. The relationship between the concrete's strain response under increasing stress. Experimentally determined.

PR - ν_c : Poisson's Ratio. Constant between axial and lateral displacement of concrete under uniaxial loading. Bright and Roberts (2010) gives the value for uncracked concrete as 0.2. This shall be used for all simulations.

ECC - Eccentricity parameter between the compressive and tensile strengths. This is calculated by LSDYNA using formula (9) from Jirásek and Bazant (2002).

QH0 - q_{ho} : Initial hardening modulus given as f_{ci}/f_c . Since 30% of f_c is generally known as the "onset of localised cracking" ie. the first yield surface and cracks begin to lengthen thereafter (Chen, 2007), the default value is given as 0.3.

FT - f_t : Uniaxial tensile strength. Determined from a combination of the experiments and simulations.

FC - f_c : Uniaxial compressive strength. Determined experimentally.

HP - H_p : Hardening parameter. A value of 0.01 was chosen as rate dependent strain was not implemented in these simulations.

AH, BH, CH, DH - A_h, B_h, C_h, D_h : Hardening ductility parameters required for the material. These use default values for both plain and permeable concrete types listed in Table 6.

AS - Ductility parameter during damage. 15 is given as the default value.

DF - D_f : Flow rule parameter. 0.85 is given as the default value.

FC0 - F_{c0} : A Rate dependent parameter that is only necessary if dependency of the strain rate STRFLG (see later) is a required attribute. The default value is 10 MPa.

TYPE - The strain softening correlation of the material response as a crack opens can be represented by multiple types of damage formulation such as linear, bilinear or exponential or no damage at all. The CDPM model typically uses bilinear softening which is specified by the value 1.0.

BS - B_s : Damage ductility exponent during damage

WF - Parameter that determines the maximum tensile damage variable calculated from the total fracture energy and the tensile strength. The type of softening regime specified determines the formulation that is used to calculate this parameter. As bilinear softening will be used, the equation is given as:

$$W_f = \frac{4.444G_f}{f_t} \quad (10)$$

where G_f is the total fracture energy and f_t is the concrete tensile strength.

If the total fracture energy is unknown, CEB-FIP (2010) recommends that it is calculated using:

$$G_f = 73f_c^{0.18} \quad (11)$$

where f_c is the measured compressive strength of concrete.

WF1, FT1 - w_{f1}, f_{t1} : Parameters that determine the softening gradients and intermediate thresholds of the bilinear softening regime. Defaults are given in Table 6.

STRFLG - Parameter that either holds the value 1 or 0 and specifies whether strain rate dependency is required in the model. This is not required here so the value specified is 0.0.

FAILFLG - Determines whether model will take erosion of the material (where fully softened elements are removed) into account during the simulation. For the purposes of consistency between tests, this will not be applied in this study by specifying a value of 0.0.

EFC - ε_{fc} : Parameter that determines the level of softening that occurs under compressive loading and the brittleness of the failure. Determined iteratively from simulations in section 5.

ISOFLAG - Determines whether an isotropic, 1, or anisotropic, 0, damage formulation is specified according to the sign of **E**. CDPM2 uses an anisotropic damage formulation as shown by formula (5) and this is specified in the test by using a positive value for **E**.

4.4 Plywood Bearing Plates Linear Elastic Model

The loading strips were also modelled as part of the simulation. As solid objects, the thin plane dimensions of these strips would mean that, when meshed, the element size would become very small. As LS-DYNA determines the time-step size based on the smallest elements in the model (explained in section 4.5), for coarser meshes, it would be these that would dictate and therefore increase the calculation time. Therefore, the plates have been modelled as shells with a specified 4 mm thickness in the code. They were initially modelled as very coarse mesh plates however this was shown to affect the failure curve behaviour so a finer mesh size of 0.005 m was used to allow for loading variation across the strips. They are generally made of plywood however the wood

model in LS-DYNA only supports solid elements so the shell mesh excludes the use of this particular material. However, since the plates are only required to distribute the load along the concrete surface, the failure properties are not of major importance. Therefore, they have been modelled as a linear-elastic material MAT_Elastic with properties similar to a typical plywood specimen. The relevant input parameters for the linear elastic input card are outlined in Table 7 and specified below.

Table 7: Input card for MAT_Elastic in LSDYNA including default values from LSDYNA Manual

Card 1	1	2	3	4	5	6	7	8
Variable	MID	R0	E	PR	DA	DB	K	
Type	A8	F	F	F	F	F	F	
Default	none	none	none	0.0	0.0	0.0	0.0	

For this simulation, properties of Plywood from Cai and Ross (2010) and Kretschmann (2010) have been implemented and the values used are listed alongside parameter descriptions.

RO - ρ_p : Plywood Bulk density - 900 kg/m³

E - E_p : Young's Modulus of plywood - 3.83 GPa

PR - ν_p : Poisson's Ratio of plywood - 0.3 (assumed)

Other inputs are not relevant for this simulation and no input values are required other than defaults.

4.5 Explicit Analysis LS-DYNA Time Step Calculation

LSDYNA splits the specified time of a simulation into many different timesteps governed by geometric and material properties of the mesh at the current timestep (Livermore Software Technology Corporation, 2002).

LSDYNA operates by calculating the acceleration and displacement of each node from nodal forces at the start of each step and solves node-by-node in a step-wise manner. The movement of each node in this timestep will cause strains and forces through elements to the surrounding nodes and these forces are used in the next timestep. Forces from loading move through the material as a form of stress wave travelling at the speed of sound of the material. Due to this wave, the timestep size is important because if it is too large, the stress wave from previously calculated nodes will reach adjacent nodes in the same timestep causing severe calculation errors.

LSDYNA checks over all the elements to determine what element will cause the shortest timestep. The element size and material are both controlling factors since a longer element in a material with a higher acoustic speed could allow a force to travel across it faster than a smaller element in a slower acoustic speed material. Therefore, the shortest time that a wave can travel across an element in the mesh is the calculated critical timestep size. To ensure computational stability, this is scaled down by a specified value in the program input defined by the TSSFAC keyword (0.8 is used in these simulations).

In Livermore Software Technology Corporation (2006), the timestep, t , is defined as:

$$t = \frac{L_{el}}{c} (\times TSSFAC) \quad (12)$$

where L_{el} is the element length or altitude (depending on the source specified) and c is the speed of sound in the material as defined by the element type. To save computational expense, a uniform mesh is recommended to stop smaller elements in uneven meshes dictating the timestep size although refining meshes in areas of interest only will still reduce the number of nodes that need to be calculated.

4.6 Displacement Load Definition

This model is intended to simulate both the peak load and post-peak response of the specimen while mimicking the experimental process. Therefore, an increasing displacement on the top loading strip has been implemented as opposed to a force so that post-peak behaviour of the concrete model with regards to stress-reduction and any secondary reloading can be recorded in the simulation. This method produces comparable results in which the suitability of the behaviour model and overall modelling process can be discussed in terms of the experimental results.

5 Simulation Analysis

5.1 Setup of Analysis

5.1.1 Modelling Strategy and Tensile Stress Calculation

To estimate the uniaxial tensile strength of the experimental concrete specimens, the model that was used to simulate the effects of constituents was created to mimic the conditions of the tensile splitting test.

As with the physical experiments, the reaction force of the lower bearing strip in the simulation was measured as a value for load applied and plotted against the displacement of the nodes of the loading strip. The peak splitting test tensile stress could then be approximated using

$$f_{t,sp} = \frac{2F_{max}}{\pi LD} \quad (1)$$

which is stated and explained as formula (1) in section 2.2.

The CDPM2 model required an input for uniaxial tensile strength, f_t , but this had not technically been found yet from the experiments. Therefore, an estimation of the conversion factor produced by the simulation, α_{sp} , between f_t , from the simulation input, and $f_{t,sp}$, from the simulation output, had to be determined.

A validation material based on conventional concrete was created to test the simulation performance and is discussed in greater depth in section 5.3.1. In summary, four different mesh sizes were used and out of these, a “fine” mesh of 0.005 m elements was selected for use in each simulation. With this mesh, a conversion factor of 1.143 was calculated, as shown in section 5.3.3.3. This was then used to factor $f_{t,sp}$ values from the experiments to gain an input value of f_t for the simulation of each concrete set. The effectiveness of this process is analysed in the discussion for each set.

5.1.2 Tensile Splitting Test Model geometry

The model geometry is identical to the concrete specimens used in the physical experiments with specimen and packing strip sizes (15mm wide and 4mm thick) from BS EN 12390-6, so an accurate comparison can be analysed. This is shown in in Figure 17.

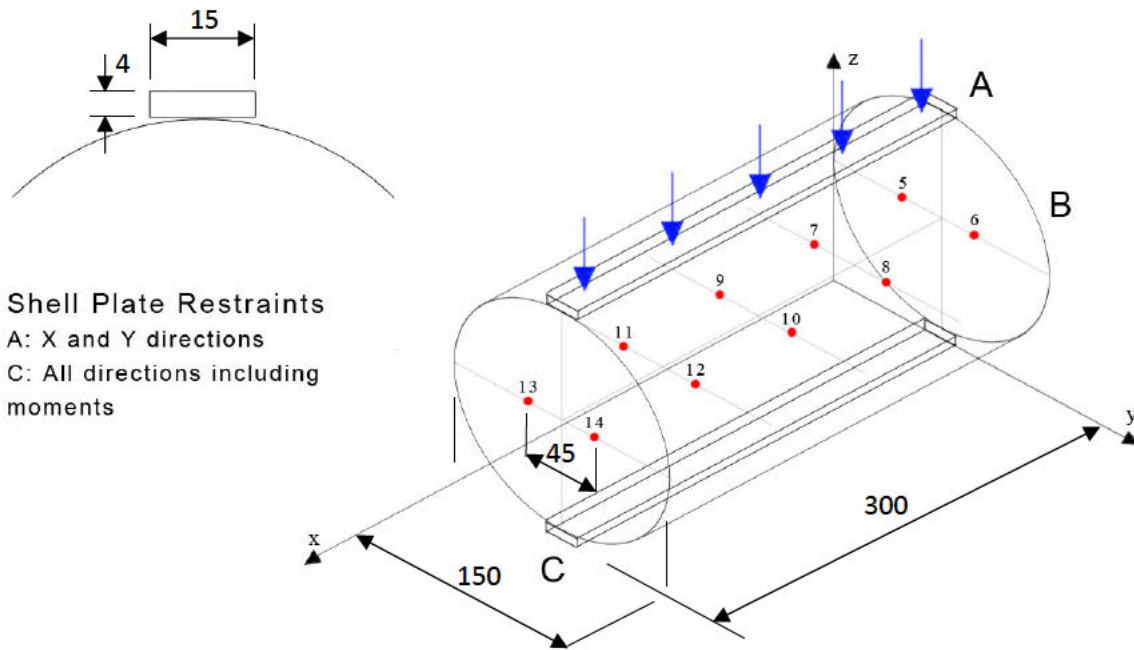


Figure 17: Tensile Splitting Test simulation geometry (all sizes in mm)

The CDPM2 material from section 4.3.2 is applied to part B, which is the concrete cylinder and consists of a “Fine” mesh using a guide element size of 0.005 m and 77027 nodes.

The plywood material and shell plate thickness from section 4.4 are applied to parts A and C, which are the loading and lower bearing strips respectively.

The displacement load is applied to all nodes on part A to give a uniform displacement of the loading strip as if it were being compressed by a testing rig. Part A is displaced incrementally from 0 to a maximum displacement of 3×10^{-3} m over a period of 0.1 seconds. This is considerably faster than a real splitting test but, as will be mentioned in section 5.3.2.1.2, should not affect the material response and results significantly. This displacement is also a large enough value to capture the failure and relevant post-peak response of the material.

Displacements of nodes 5-14 were monitored over the loading period to compare the crack width with the experimental observations. Multiple pairs of nodes were created in the mesh to allow for analysis of different crack widths and responses along the length of the specimen if required. The nodes were 45mm apart equidistant from centre and any significant increase in this distance would indicate the width of the widening crack. For comparison at different time steps, the crack widths for all node pair were averaged.

5.1.3 Strip Contact Definition

The contact between the bearing strips and the concrete cylinder is key to the model. The actual frictional value between the strips and the specimens would be very difficult to calculate and would

not be the same for every sample due to the variability between samples. So, to ensure that the model does not become unstable early during loading through force balance hysteresis, a low static friction coefficient of 0.1 was applied.

5.1.4 Deriving Inputs for Permeable Concrete CDPM2 Behaviour Models

CDPM2 has many “default” input values that have been determined as a result of calibration from past investigations and have been proved experimentally to provide accurate response patterns for conventional concrete (Grassl et al, 2013). Some of these parameters are not easy to determine unless significant testing is undertaken which is outside the scope of this study. Fitting the experimental data as closely as possible may not give a realistic reflection of the true parameter values as information from the experiments is limited. However, some input parameters such as compressive and tensile strength can be easily estimated from standard material testing, such as in section 3, without having to go through a long iteration process. Part of the premise of the modelling element for this project is to determine whether the current CDPM2 model, with the complex “default” parameters, and a simplified homogeneous mesh can be used to describe the response of permeable concrete by only changing the easily obtainable parameters. Then, it can be determined whether only changing these parameters is enough to reasonably describe the observed behaviour using CDPM2 and a homogeneous mesh or whether more complex analysis methods are required. This does not obscure the main goal of determining estimate values for the uniaxial tensile strength.

With the rest left as default values, the parameters altered and their sources were:

- **RO** - ρ_c : Concrete bulk density. Determined from weighing of the samples after moulding
- **E** - E_c : Young’s Modulus. Determined from the positive gradient of the load vs displacement compression loading curve after points are converted into stress and average strain respectively.
- **FT** - f_t : Uniaxial tensile strength. Experimental splitting tests gave a value of the splitting test tensile stress, $f_{t,sp}$, at the peak of the force vs loading plate displacement curve for each mix. This is multiplied by the conversion factor, α_{sp} , as explained, to give an estimation of f_t .
- **FC** - f_c : Uniaxial compressive strength. Determined from the peak of the compression stress vs strain curve.
- **ECC** - Eccentricity parameter between the compressive and tensile strengths. Changes according to f_t and f_c using formula (9).
- **WF** - w_f : Parameter that determines the maximum tensile damage variable.
 - ◆ Set 1 and 2 - Estimated from formulae (10) and (11) as outlined in section 4.3.2.
 - ◆ Set 3 and 4 - Estimated using $w_f = \frac{Fibre\ Length}{2}$ (N/m)
 - ◆ For Set 3 and 4, **WF1** will remain as the value used for Set 1 and 2 respectively.

- **EFC** - ϵ_{fc} : Parameter that determines the level of softening that occurs under compressive loading and the brittleness of the failure. The only iterated value determined during the simulation process, gained by fitting the simulated compression response to the immediate gradient of the line after compressive failure.

Material parameters were tested and calibrated against the experimental results using compression single element simulations. The results of the experimental compression cube tests were reasonably consistent and input parameter values for each specimen from each mix could be extracted. These values were then averaged and used as material input parameters for each simulation set. For comparison, the compression results have been converted into a compressive stress vs average strain form as explained in section 3.4.1.1. While it was not entirely correct to present the results in this form before, now the goal is to describe the material in a homogeneous sense with values averaged over the volume so that representative model values can be extracted.

Since a uniaxial tensile test was not performed, tension single element tests were performed only to ensure that the loading and failure curve gave reasonable expected results from the inputs and that there were no major calculation errors. The tensile stress was plotted against the displacement load, not the strain, again due to localised failures occurring. This should not affect the single element test as only one element is loaded and the whole mesh will fail at once however for consistency, the result is presented in this way.

The geometry of the single element tests are shown in Figure 18. Since Lockhart (2017) has already proved that the element size has little to no effect on the compression and tensile response using the CDPM2 model, only one test, using a cube of 50 mm sides, was performed for tension and compression of each material set. The input and mesh files are available from Grassl (2017).

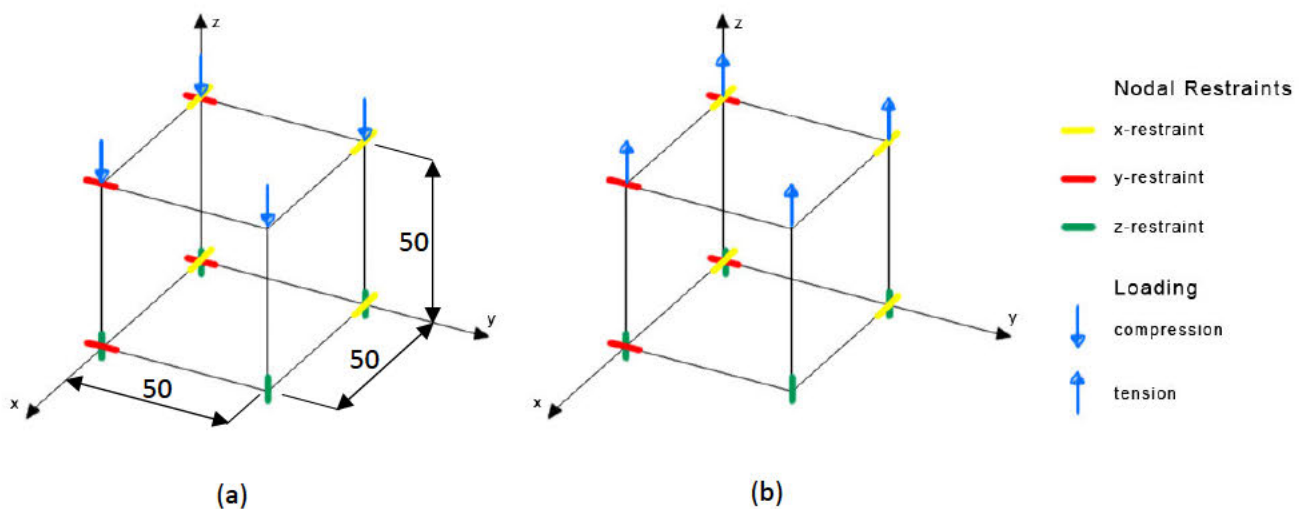


Figure 18: Geometry, loading and restraints of the (a) compression and (b) tension single element tests (all sizes in mm)

5.2 Set Specific Inputs, Results and Discussion

5.2.1 Set 1

Set 1 relates to the plain 20 mm aggregate permeable concrete and the altered input parameters used are shown in Table 8. It was not necessary to alter the ϵ_{fc} value as Figure 19 shows that the single element compression results obtained with the default value show good agreement with the experimental compression results. Other input values were altered with reference to section 5.1.4.

Table 8: Set 1 derived input parameters (including defaults)

Variable	MID	RHO	E	PR	ECC	QHO	FT	FC
Value	1	1.856e3	3e9	0.2	0.536	Default	1.3e6	8.53e6
Variable	HP	AH	BH	CH	DH	AS	DF	FC0
Value	0.01	Default	Default	Default	Default	Default	Default	Default
Variable	TYPE	BS	WF	WF1	FT1	STRFLG	FAILFLG	EFC
Value	1	Default	367.2e-6	Default	Default	Default	Default	1e-4

5.2.1.1 Single Element Tests

5.2.1.1.1 Results

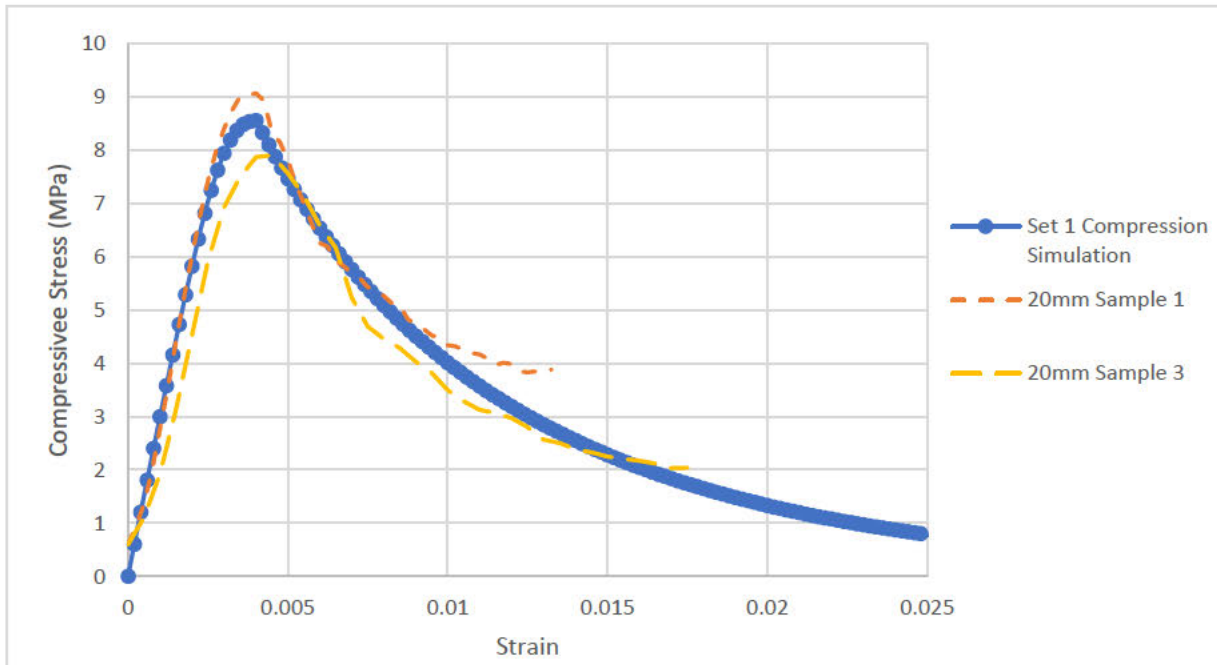


Figure 19: Set 1 Single Element Compression Test and Experimental Samples stress vs strain results

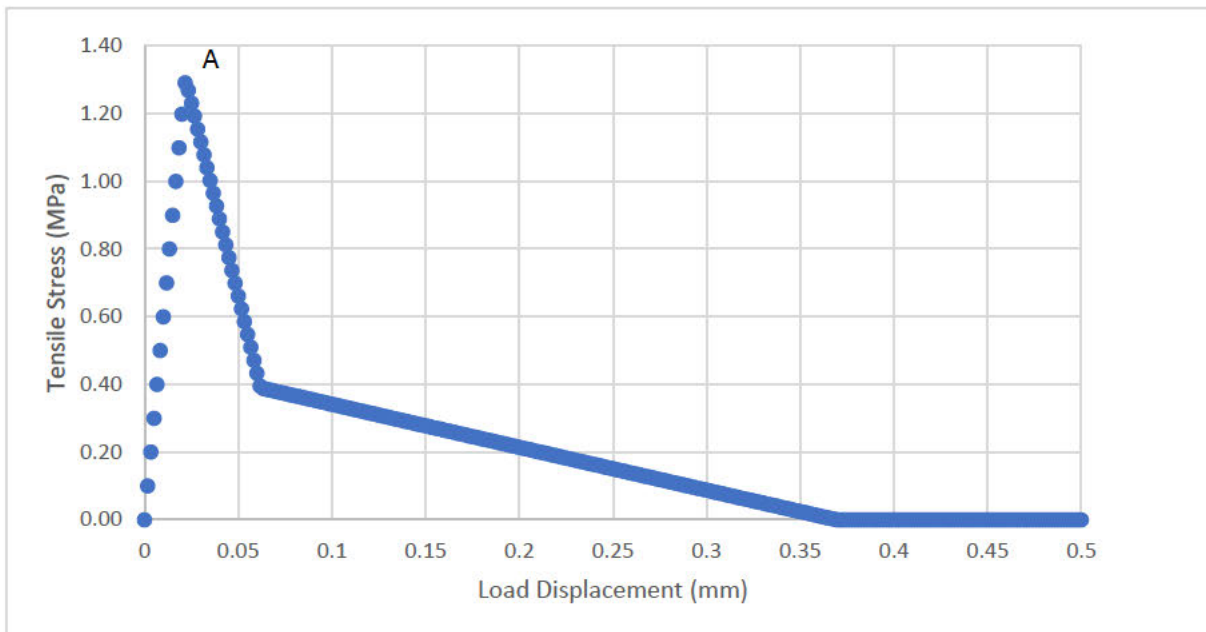


Figure 20: Set 1 Single Element Tensile Test stress vs displacement results

5.2.1.1.2 Discussion

It can be seen in Figure 19 that the single element compression results agree with the experimental results well during the initial loading and immediate post-cracking periods. As is to be expected, the stress gradient matches the results from which it was derived and the failure “strain” agrees with the experimental samples by failing at around 0.004. For extra confidence, this also is consistent with the results gained in the investigation by Deo and Neithalath (2010). The compressive strength is also a direct model input so the fact that the simulated strength lies between the two samples at the average is not surprising. The other factor that has a major effect on this simulation is ϵ_{fc} . This can only really be deduced to the point where the post-peak gradients match and in this simulation, the response was very similar immediately after cracking with the default value. This value is generally for quite brittle responses (Grassl, 2016) which seems appropriate for a material that can undergo rapid crack propagation and instability.

Where the response begins to deviate is at around a “strain” of 0.01 where the experimental sample responses begin to flatten out significantly and the simulated single element continues to fall asymptotically towards 0. The main reason for this is most likely that the single element test for CDPM2 is simulating a perfect response of a single particle of homogeneous material where the response will always rely on the input values with no influence from other factors encountered in experimental testing. The physical samples tested are not homogenous and the material inputs of the model that average out all the irregularities, voids and different ingredients do not represent the actual mechanisms occurring under extreme strain. The void content is so large that it can be described as a part of the material that provides no resistance to loading and this impacts the stiffness and other parameters of the bulk material. This also means that the strength and stiffness

of the aggregates separately are not represented by the material inputs gained and are not accounted for when only a single homogeneous element is simulated. As the central aggregates are squeezed together, crushing of these becomes the main failure mode as they are held in place by the outer aggregates until these fall off. This results in a decreased softening response. As is seen in Figure 8(a), these samples disintegrated with many sections cracking off the side, reducing the loading area. Therefore, the total applied force continues to decrease slowly but this cannot be described with a simplified single element simulation. The material will perfectly deform according to the input parameters and ignore aggregate strength or processes such as disintegration.

The uniaxial tension single element test in Figure 20 shows the bi-linear softening feature of CDPM2. All results here directly relate to the input parameters and could be used in future should uniaxial tensile tests of similar materials be performed. In particular, the stress value at point A exactly corresponds to the value of f_t from the input parameters and is calculated as described in section 5.1.1. Where the stress reaches 0 also relates well to the value of w_f .

5.2.1.2 Simulated Tensile Splitting Test

5.2.1.2.1 Results

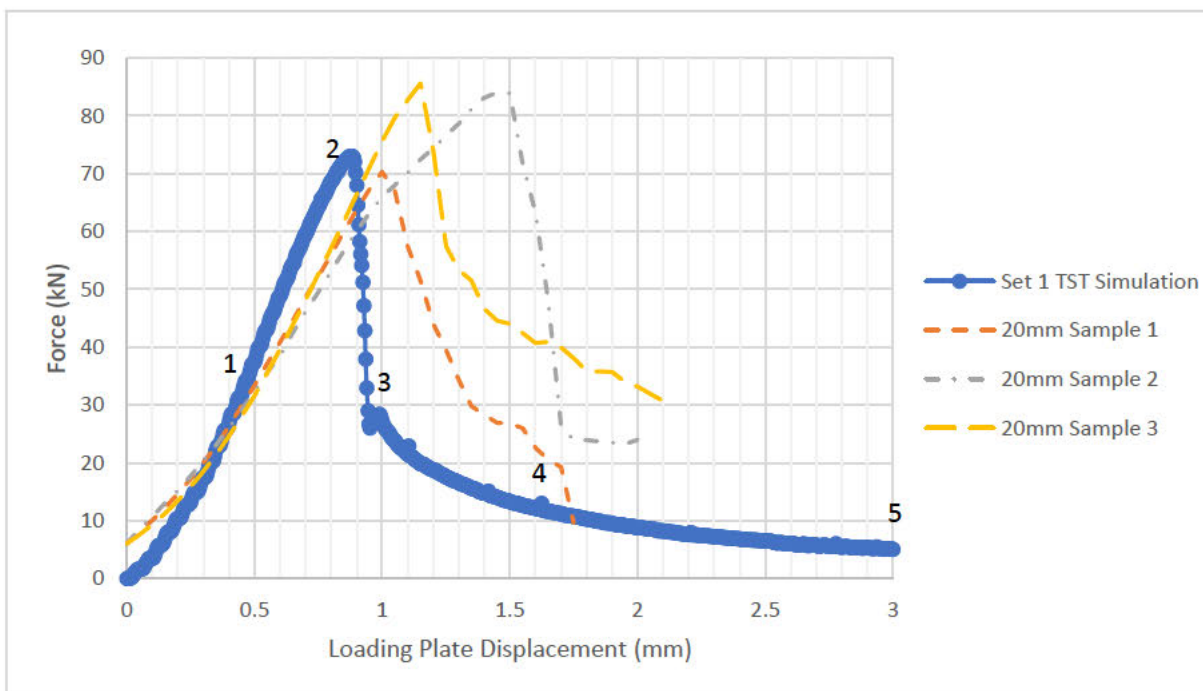
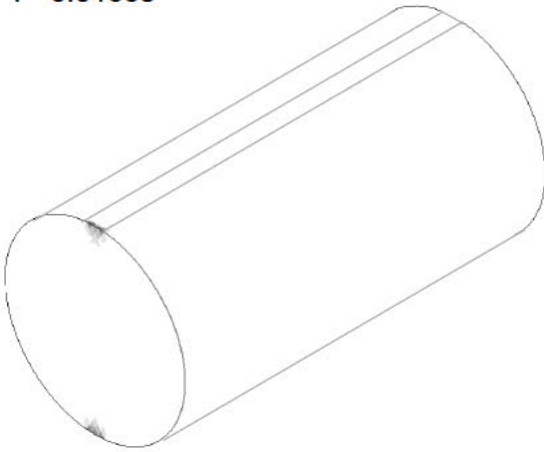


Figure 21: Set 1 Computational and Experimental Tensile Splitting Test (TST) force vs plate displacement response

Crack Pattern Stages

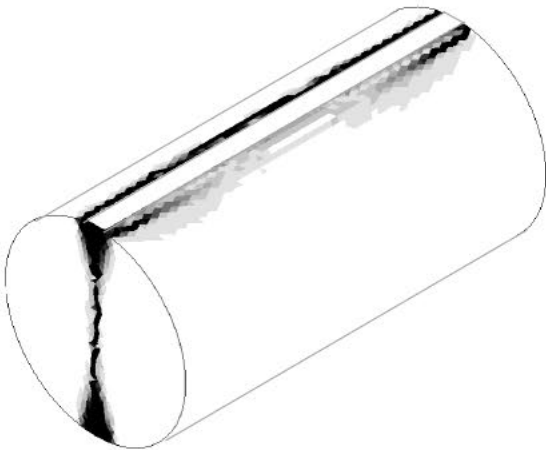
1 - 0.0133s



2 - 0.0267s



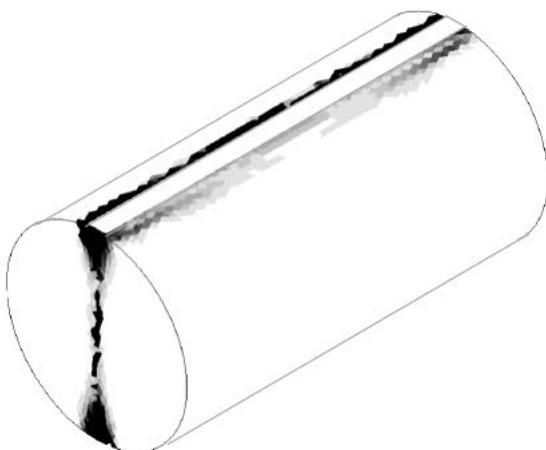
3 - 0.0333s



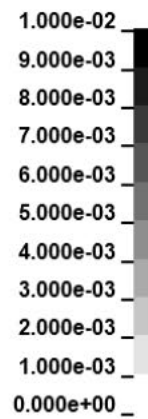
4 - 0.0533s



5 - 0.1s



Strain



Average Crack Width

Stage	Crack Width (mm)
1	0
2	0
3	0.37
4	0.87
5	2.14

Figure 22: Set 1 Progressive Crack Pattern

5.2.1.2.2 Discussion

The splitting test simulation model for set 1 in Figure 21 produces a general shape that looks reasonable given the experimental results although there is some question as to what some of the features represent.

The failure load predicted is reasonably accurate and lies within the experimental observed failure loads. This shows that the conversion process for predicting the uniaxial tensile stress of these samples is based on a decent estimate for conversion factor α_{sp} .

Initially, the loading curve in Figure 21 rises more steeply than the experimental results and therefore, the simulated specimen fails before the experimental specimens in terms of loading plate/strip displacement. This is not entirely unreasonable since the simulation produces a perfect contact between the sample and the loading strips while the experimental samples do not have smooth sides and have numerous voids visible on the surface. The load is therefore not transferred as efficiently so the load rises more slowly which cannot be captured by the homogeneous simulated mesh. However, the actual pre-peak response shape is generally accurate.

The immediate drop-off after failure is very steep in the simulation and considerably steeper than what is observed in the experimental samples. This period represents the opening of the main tensile crack through the specimen and shows that failure is very sudden and complete in the simulation as opposed to the experimental specimens that seem to soften in a more ductile manner. This, again, may be due the homogeneity of the mesh. In the experiments, the central crack will be opening as the plate is pushing down on the sample however the size of the aggregates is much larger than the opening crack. Therefore, the aggregates will still be interlocked in some manner and able to transfer vertical load for a short period after cracking. In the mesh, there is no aggregate interlock so once the elements have failed, there can be no load transfer through the central split and this area is essentially redundant for loading as the strip compresses it. The difference between the responses is not large but significant enough to say that these interlock processes during the splitting failure are missed.

The load immediately after failure is similar to samples 1 and 2 but sample 3 is significantly different. It is important to note that the failure mode of sample 3 was unconventional while the others were as expected. It is not surprising that the similar strip contact area between the simulation and the experiments produced similar loads at this point. However, further experimental post-peak behaviour is much less consistent and therefore, the effectiveness of the simulation cannot be commented on other than producing a much smoother response.

In Figure 22, the crack-pattern evolution is shown at the loading displacements highlighted by the numbers in Figure 21. The strains that are induced in the material mesh as the loading displacement increases show areas of high displacement when compared to the size of each

element. As would be expected in a real splitting test, strains initially occur underneath the loading plates, as shown in pattern 1, as the compressive forces here are much greater than any central tensile forces induced at this stage.

As the specimen nears failure in pattern 2, the strains propagate through the middle of the sample away from the loading plate indicating that the tensile forces have now significantly increased. However, the strain underneath the loading plates is still dominant and tensile failure has not occurred.

In stage 3, just after failure, a crack has propagated right through the centre of the sample which is desirable in the sense that the real splitting test failure mode occurs here. However, as explained before in section 3.4.2.3, this failure will still mean that the splitting test method does not represent the post-peak tensile cracking response.

Aside from that, the wedge behaviour observed in the experiments is visible here with a triangle of large strains building up between the central crack and the loading strips. These wedges seem to have less of an effect in prising the specimen apart over time than in the experiments as can be seen in stages 3, 4 and 5 where the crack only widens to 2.14 mm at much greater strip displacement rather than the 6 mm observed from the experimental specimen. This could be due to the same process that occurred when the single element test was compared to the compression test. The stiffness and strength of the aggregates are averaged out by the voids and are mixed into one homogeneous material that upon failure, can carry no load. As crushing occurs in the experiments under the loading strips, the bonded aggregates still physically exist to prise the specimen apart as they are pushed inwards whereas in the simulation, there is no physical representation of this effect. Since the material has likely completely failed by this point, the damage model dictates that it can infinitely deform without carrying any stress. The thin loading strip can move into the cylinder without forcing the sides apart significantly. This is also likely the reason why the measured load still decreases as well. As the material progressively fails, fewer and fewer elements are able to carry any stress as they are fully damaged. In the experiments, this load decrease is partly due to the continuing material failure but also due to the loading area decreasing significantly as the cylinder halves are forced apart. An extra point is that there is also no gravity in the simulation to allow the sides to fall away naturally so they remain in position which further inhibits any increase in crack width not due to loading.

5.2.2 Set 2

Set 2 relates to the plain 10 mm aggregate permeable concrete and the altered input parameters used are shown in table 9. The ϵ_{fc} value was adjusted downwards for a steeper initial softening response so that the single element simulation represented the compression response found in the experiments, shown in Figure 23, more accurately.

Table 9: Set 2 derived input parameters (including defaults)

Variable	MID	RHO	E	PR	ECC	QHO	FT	FC
Value	1	1.91e3	5.937e9	0.2	0.520	Default	1.61e6	18.82e6
Variable	HP	AH	BH	CH	DH	AS	DF	FC0
Value	0.01	Default	Default	Default	Default	Default	Default	Default
Variable	TYPE	BS	WF	WF1	FT1	STRFLG	FAILFLG	EFC
Value	1	Default	341.1e-6	Default	Default	Default	Default	0.56e-4

5.2.2.1 Single Element Tests

5.2.2.1.1 Results

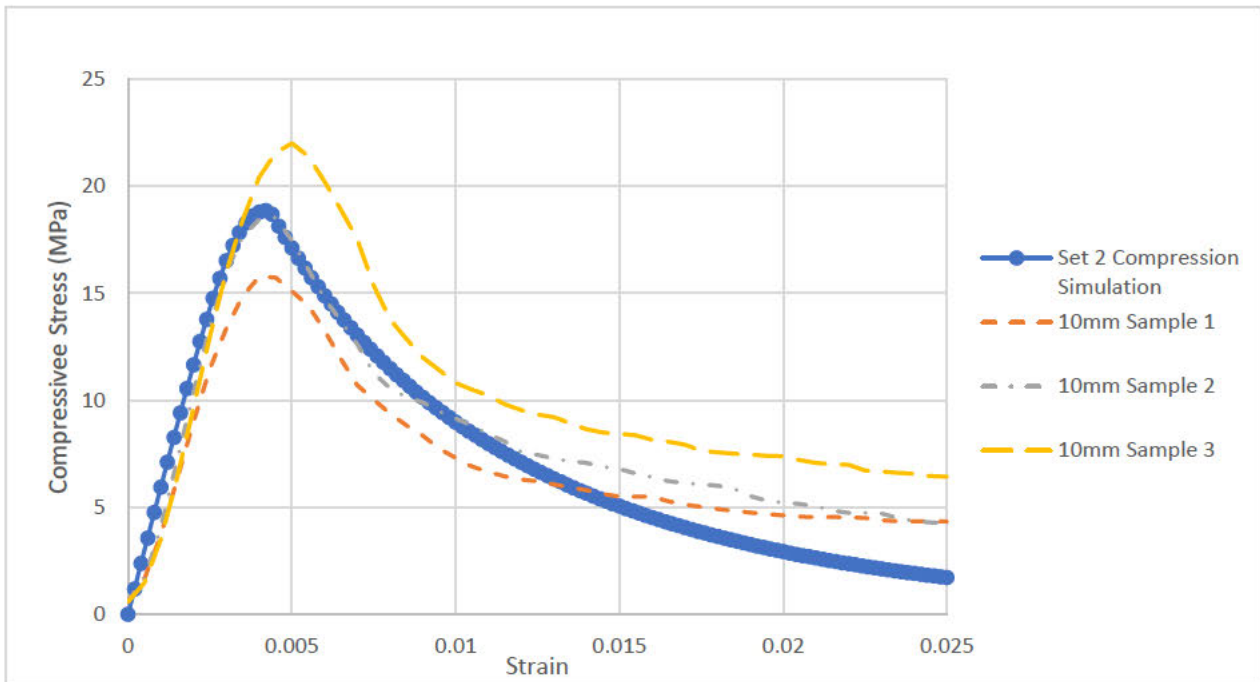


Figure 23: Set 2 Single Element Compression Test and Experimental Samples stress vs strain results

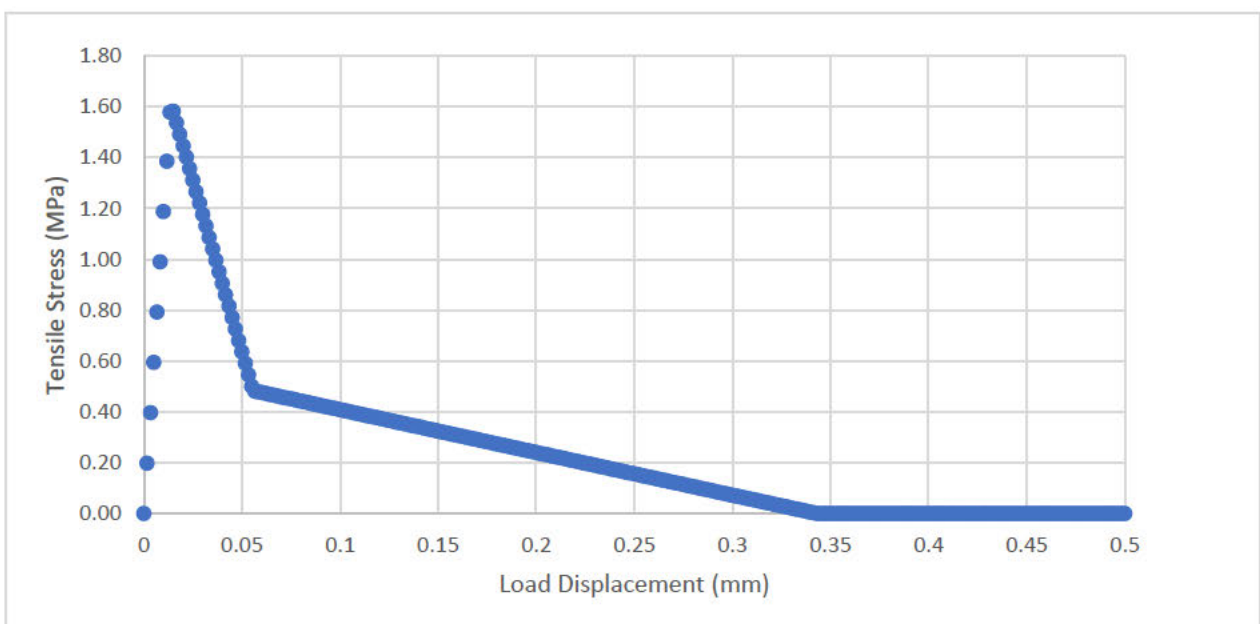


Figure 24: Set 2 Single Element Tensile Test stress vs displacement results

5.2.2.1.2 Discussion

Similar behaviour is noted in the compression single element test as for set 1. As can be seen in Figure 23, the CDPM2 model allows the stress to asymptotically fall to zero while the stress in the real compression cubes levels out well above this value and decreases very slowly. Other than that, the behaviour of these model inputs, again, matches the experimental results well.

Figure 24 shows the tensile behaviour as performing as expected. The maximum tensile stress matches the f_t model input well and again, w_f relates well to where the stress reaches 0.

5.2.2.2 Simulated Tensile Splitting Test

5.2.2.2.1 Results

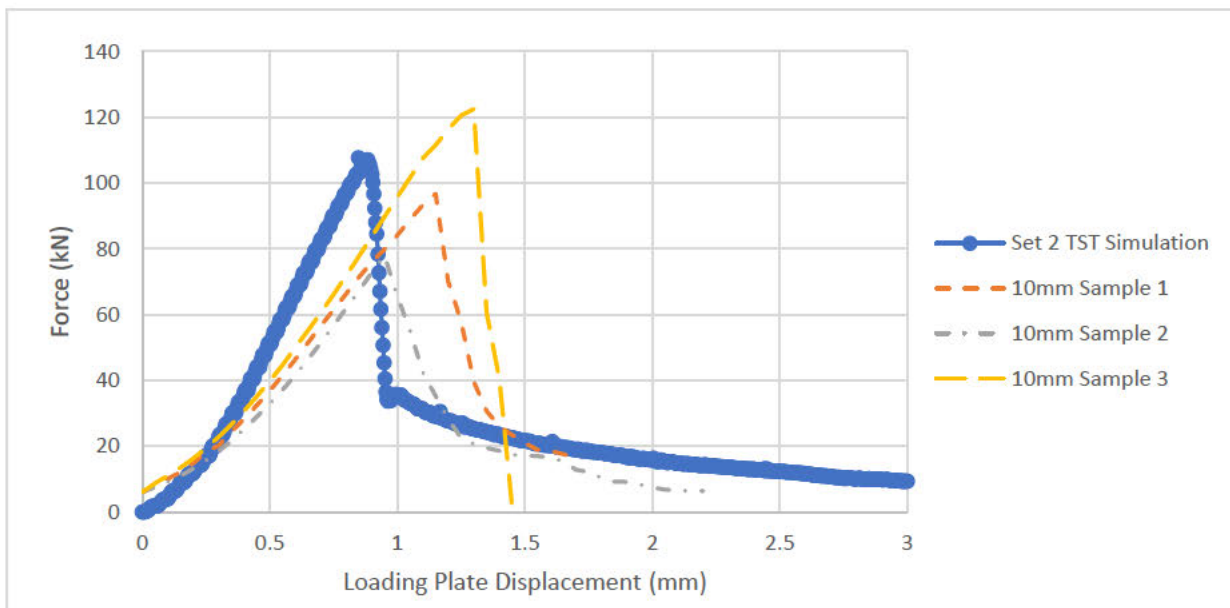


Figure 25: Set 2 Computational and Experimental Tensile Splitting Test force vs plate displacement response

5.2.2.2.2 Discussion

As shown in Figure 25, much of the same behaviour that occurred in the simulation of Set 1 occurs for Set 2. Once again, the sample fails at a smaller plate displacement than the experimental samples but with a similar load. The general shape is also very similar but now, the post-peak behaviour found in the experiments is much more consistent and is therefore represented a lot more accurately by the simulation. As previously implied, the 10 mm aggregate material is more homogenous with fewer voids and distinct irregularities so it behaves more like conventional concrete than the 20 mm aggregate material. This is closer to the material and mesh model that the simulation represents and so it makes sense that this should occur. There are still discrepancies however which are caused by the remaining aggregate interlock, although this effect is much reduced in the smaller aggregate. Therefore, even though the immediate softening is still too sharp, aside from a comparison with sample 3 which unexpectedly failed entirely very rapidly,

the deviation from the experimental results is lessened. Many more physical samples would have to be tested to ensure that this response is a more reliable representation of potential experimental findings.

5.2.3 Set 3

Set 3 relates to the fibrous 20 mm aggregate permeable concrete and the altered input parameters used are shown in Table 10. The ϵ_{fc} value was again changed in this set to allow for representation of the more brittle compressive failure response observed for this mix in Figure 26. As mentioned in section 5.1.4, w_{f1} remains the same value as it was for set 1 so that the tensile response immediately after cracking remains very similar. Technically, the value of f_{t1} has changed though as the default formula in LS-DYNA calculates it as 30% of f_t .

Table 10: Set 3 derived input parameters (including defaults)

Variable	MID	RHO	E	PR	ECC	QHO	FT	FC
Value	1	1.896e3	4.40e9	0.2	0.523	Default	1.53e6	15.03e6
Variable	HP	AH	BH	CH	DH	AS	DF	FC0
Value	0.01	Default	Default	Default	Default	Default	Default	Default
Variable	TYPE	BS	WF	WF1	FT1	STRFLG	FAILFLG	EFC
Value	1	Default	0.0175	5.507e-5	Default	Default	Default	0.60e-4

5.2.3.1 Single Element Tests

5.2.3.1.1 Results

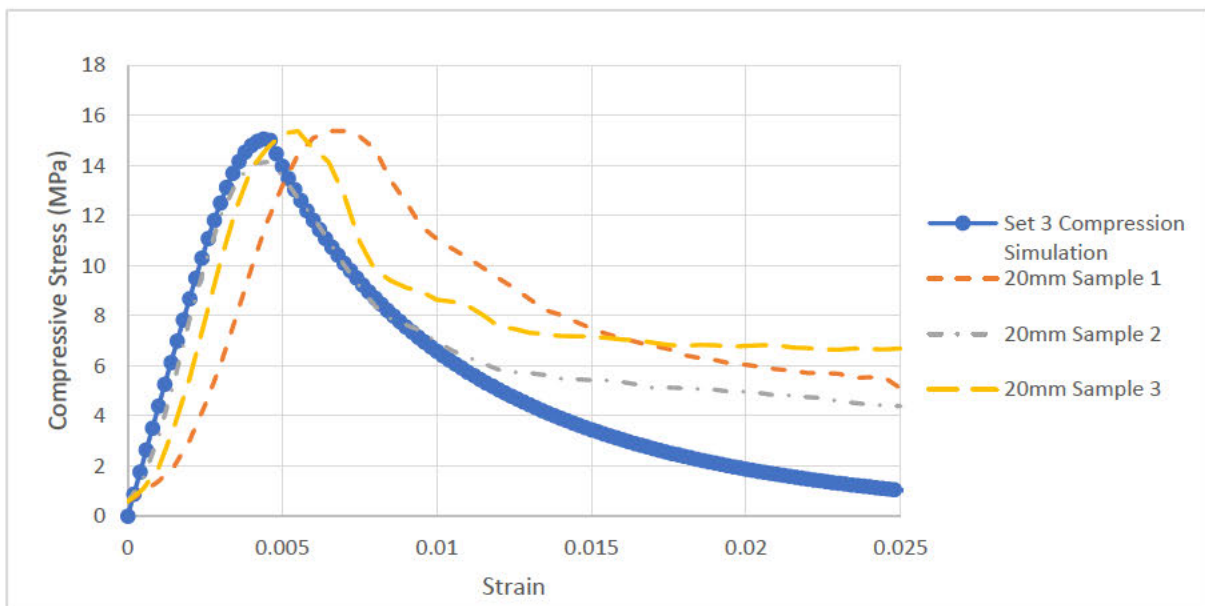


Figure 26: Set 3 Single Element Compression Test and Experimental Samples stress vs strain results

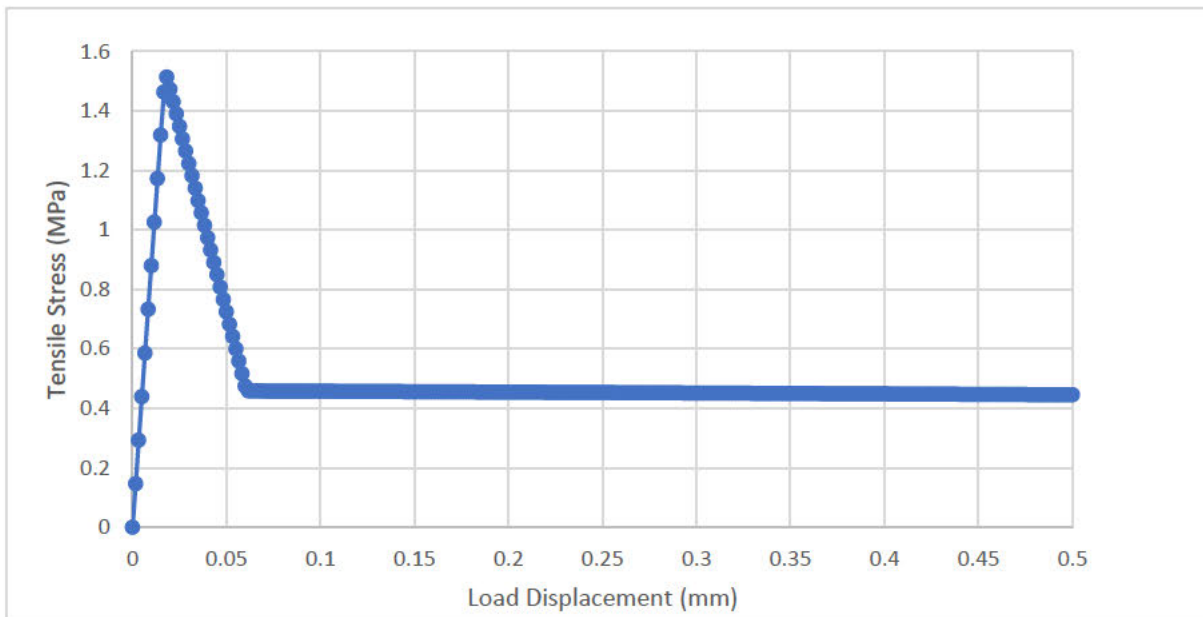


Figure 27: Set 3 Single Element Tensile Test stress vs displacement results

5.2.3.1.2 Discussion

In Figure 26, the single element test is once again in decent agreement with the experimental results. There is more observable plastic strain occurring in the experimental samples before failure than is accounted for in the simulation due to the bridging effect of the fibres. The material model can be changed to represent this by altering the B_h parameter as explained in Grassl and Jirásek (2006). However, it was decided that the response was close enough using the default value that it was not a parameter that requires calibration for every set.

The biggest visible change is in the tensile response of Figure 27 due to the estimation of the w_f damage parameter that simulates the effects of adding the steel fibres. The curve becomes almost flat after the maximum post-cracking stress however it still does drop slowly to zero after a long period. The tensile single element test is the only simulation where the w_f parameter will have any objective effect and there are no experimental results to directly compare it to. Therefore, in future, uniaxial experimental tests on permeable concrete, both with and without fibres, would be desirable since w_f is a significant damage parameter that cannot be analysed.

5.2.3.2 Simulated Tensile Splitting Test

5.2.3.2.1 Results

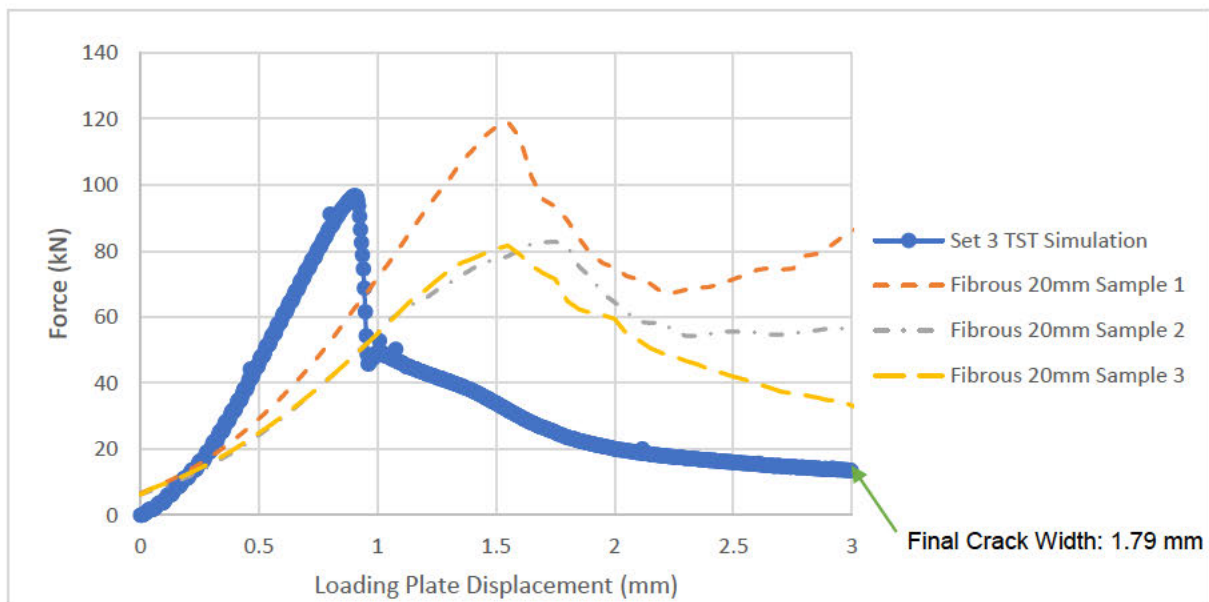


Figure 28: Set 3 Computational and Experimental Tensile Splitting Test force vs plate displacement response

5.2.3.2.2 Discussion

From Figure 28, many of the same simulated features are visible in comparison to the experimental results as before. Failure is still earlier than observed in the experimental samples but the softening response is now significantly steeper than the experimental observations. However, the actual failure load is again reasonable and within the bounds of the experimental results. The main change in the post-peak response shape is that the decrease in load is not a single smooth curve. While the load is still decreasing, there is a distinct lump visible just after the main failure has occurred. This demonstrates the inability of the simulation to represent the tensile post-peak behaviour properly as this is the only evidence visible in the simulation of the vastly increased w_f and fracture energy whereas the effects are clear in the uniaxial tension single element test.

This simulation also does not accurately produce the loading and cracking effects of the sample remaining together due to the fibres. Once again, the inhomogeneous physical mesh of the specimens, this time with fibres, cannot be truly accounted with a homogeneous mesh. When the simulated material cracks, failed material cannot carry any load as it is compressed further and is essentially redundant. When the experimental specimen cracks, only the aggregate cement bond breaks and the fibres begin utilising their tensile strength. They hold the sample together and enable further load from the strip to be transferred after cracking as explained in section 3.4.2.3. The final crack width, most likely by coincidence, is more representative of the experimental crack width. However, the value of 1.79 mm is now larger than the approximate experimental observation of around 1.5 mm. This is again due to the individual mechanical properties of the fibres not being considered separately as the load they carry in the experiments is not significant enough to cause large strains or pull-out and they continue to restrict the crack width.

5.2.4 Set 4

Set 4 relates to the fibrous 10 mm aggregate permeable concrete and the altered input parameters used are shown in Table 11. Interestingly, ϵ_{fc} , had to be increased to fit the compression results.

Table 11: Set 4 derived input parameters (including defaults)

Variable	MID	RHO	E	PR	ECC	QHO	FT	FC
Value	1	1.956e3	7.12e9	0.2	0.519	Default	2.19e6	26.78e6
Variable	HP	AH	BH	CH	DH	AS	DF	FC0
Value	0.01	Default	Default	Default	Default	Default	Default	Default
Variable	TYPE	BS	WF	WF1	FT1	STRFLG	FAILFLG	EFC
Value	1	Default	0.0175	5.116e-5	Default	Default	Default	0.65e-4

5.2.4.1 Single Element Tests

5.2.4.1.1 Results

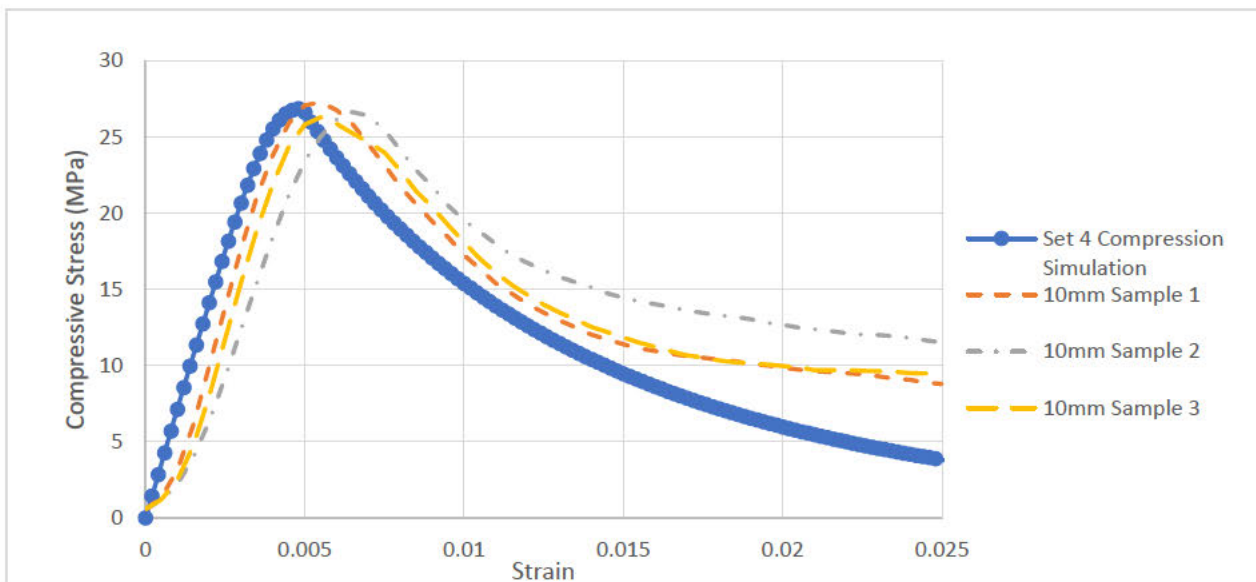


Figure 29: Set 4 Single Element Compression Test and Experimental Samples stress vs strain results

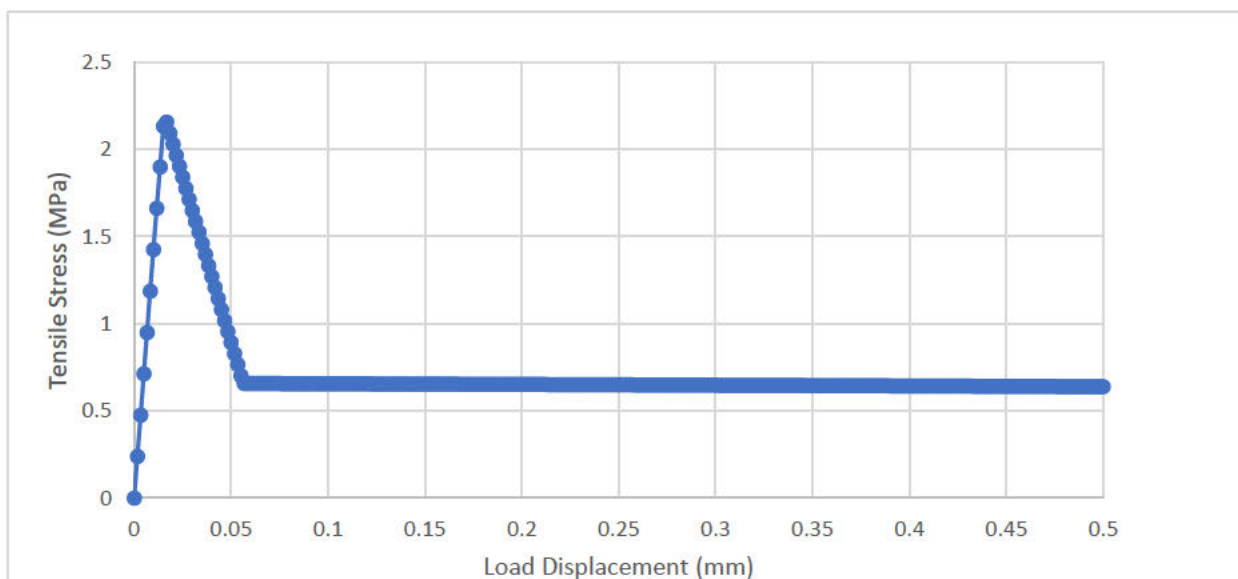


Figure 30: Set 4 Single Element Tensile Test stress vs displacement results

5.2.4.1.2 Discussion

The results for the compression experimental samples for set 4 were very tightly clustered as shown in Figure 29. Accounting for the initial contact finding in the compression tests, the updated parameters for set 4 still give a good response curve aside from the aforementioned high strain behaviour due to the single element mesh. Again, slightly more plastic straining is occurring in the experiments than in the single element test but it is not a gross estimation or simplification to leave B_h at the default value again.

The tensile single element test in Figure 30 shows a very similar response to the Set 3 with the w_f parameter causing a long displacement required to completely fail the element. The values of tensile stress and post-cracking tensile stress still match the parameter inputs of f_t and f_{t1} respectively as expected.

5.2.4.2 Simulated Tensile Splitting Test

5.2.4.2.1 Results

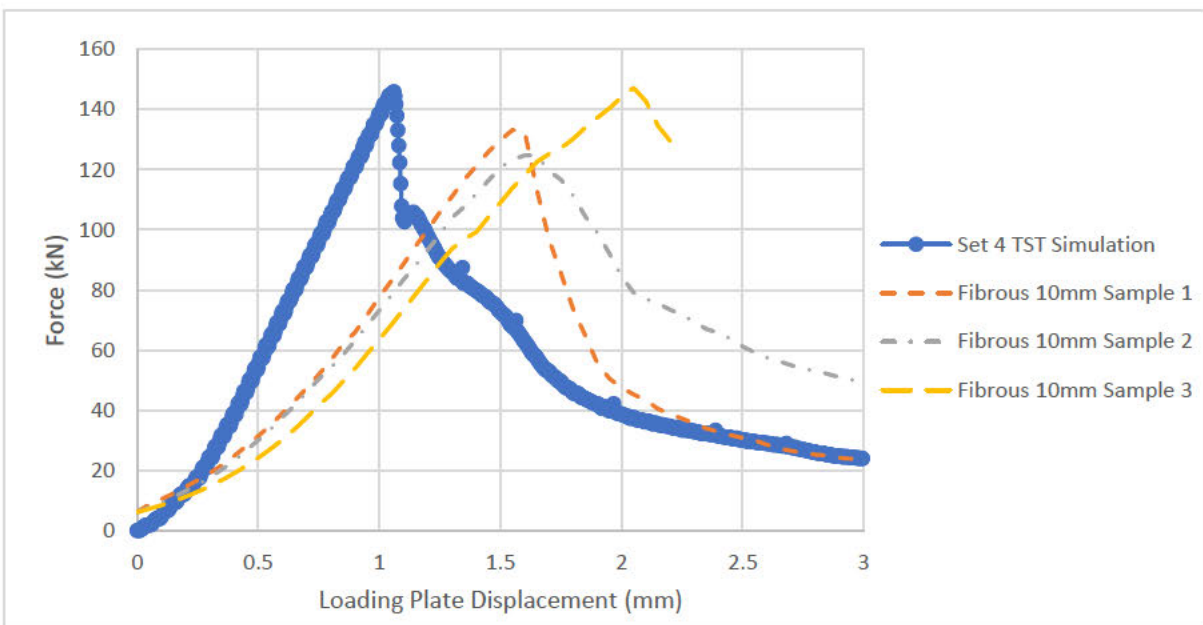


Figure 31: Set 4 Computational and Experimental Tensile Splitting Test force vs plate displacement response

5.2.4.2.2 Discussion

The comparison of the pre-peak loading to the experimental results in Figure 31 is similar to other sets. However, the failure load falls on the higher end of the measured results on this occasion. Due to the small number of samples tested, this is still within the realm of experimental error and is not necessarily significant.

The post-peak response is more interesting in its features. The lump that also occurs in set 3 is visible again but where the main crack propagation ends is the significant change. It occurs at a proportionally much higher load for this material parameter set and the immediate post-peak shape only bears minor resemblance to the experimental results. However, the shape at very high displacements seems to correspond reasonably well to the two experimental samples that did not fail completely. Unfortunately, given that the experimental post-peak responses are so inconsistent, no real conclusions can be drawn about the overall success without more testing although it is likely that similar conclusions can be drawn about the effects of the homogeneous mesh as before.

5.2.5 Permeable Concrete Results Summary

In summary, while this simulation does capture the general failure behaviour, the inhomogeneity of the experimental samples means that many of the actual processes of both the loading and post-peak response are generally missed. The mechanical properties of the individual constituents being averaged into a material mesh and model that does not physically represent them as existing separately does not seem to produce completely comparable results. This is not essentially a problem with the behaviour model itself but more an issue with the use of a homogenous mesh together with the tensile splitting test which cannot capture the tensile failure and post-peak response of the material. More representative results may be achieved in this simulation when compared with normal concrete specimens and parameters where the complete mesh is a better approximation of a predominantly solid material matrix.

5.3 Model Validation and Objectivity of Results

Before the permeable concrete specimens were simulated, a study of the model performance was undertaken on an arbitrary conventional concrete material to initially ensure that consistent and usable results were generated by the geometric mesh and CDPM2 model. Mesh dependency and time dependency were the focus so that results could be contextualised within the loading rate and homogeneous mesh assumptions made. An estimation of the tensile strength conversion factor produced was also determined for use in the final permeable concrete simulations in section 5.2.

From initial attempts, the simulation was found to be very sensitive to the type of contact with loading strips specified and small changes in mesh geometry. Therefore, for validation purposes, it was not expected that the same response would be produced for every alteration. However, the general behaviour and shape of each response pattern had to be in general keeping with responses found in the physical experiments and in literature. They also had to be explainable in the sense that if any changes occur due to the mesh or time changing, there should be plausible

reasons that these occur and these explanations should not invalidate the entire model. Taking this into account would help to prove the simulation is operating correctly within reasonable bounds. A further goal of these validations was to prove that coarser meshes and shorter loading applications could be used to reduce the length of each simulation and save on computational expense.

5.3.1 Setup

A standard validation material was created to test the response of the simulation. This material did not have any physical counterpart in the experiments but was generated based on typical values that may be found for a conventional concrete sample. These parameters are shown in Table 12.

Table 12: Validation concrete material input parameters

Variable	MID	RHO	E	PR	ECC	QHO	FT	FC
Value	1	2.4e3	20e9	0.2	0.523	Default	2.4e6	24e6
Variable	HP	AH	BH	CH	DH	AS	DF	FCO
Value	0.01	Default	Default	Default	Default	Default	Default	Default
Variable	TYPE	BS	WF	WF1	FT1	STRFLG	FAILFLG	EFC
Value	1	Default	103.7e-6	Default	Default	Default	Default	1e-3

To investigate the mesh and time dependency, four different mesh sizes for the concrete cylinder (Part B in Figure 17) were used. A coarse mesh of element size 0.02 m (1489 nodes), a medium mesh of 0.01 m elements (10447 nodes), a fine mesh of 0.005 m elements (77027 nodes) and an extra-fine mesh of 0.0025 m elements (587656 nodes). For the bearing strip shell elements (Parts A and C in Figure 17), a mesh size of 0.005 m was used to ensure stress changes across the loading strips could be captured. The specified simulation time was set at 0.1 seconds with a longer test on the fine mesh set at 1 second. The final load displacement was set at 3×10^{-3} m.

Two different failure attributes were monitored: (a) the reaction load on the lower bearing strip plotted against the loading strip displacement and (b) the crack pattern observed. Results for (a) are given in Figure 32 and results for (b) are given in Figure 33.

5.3.2 Loading Results

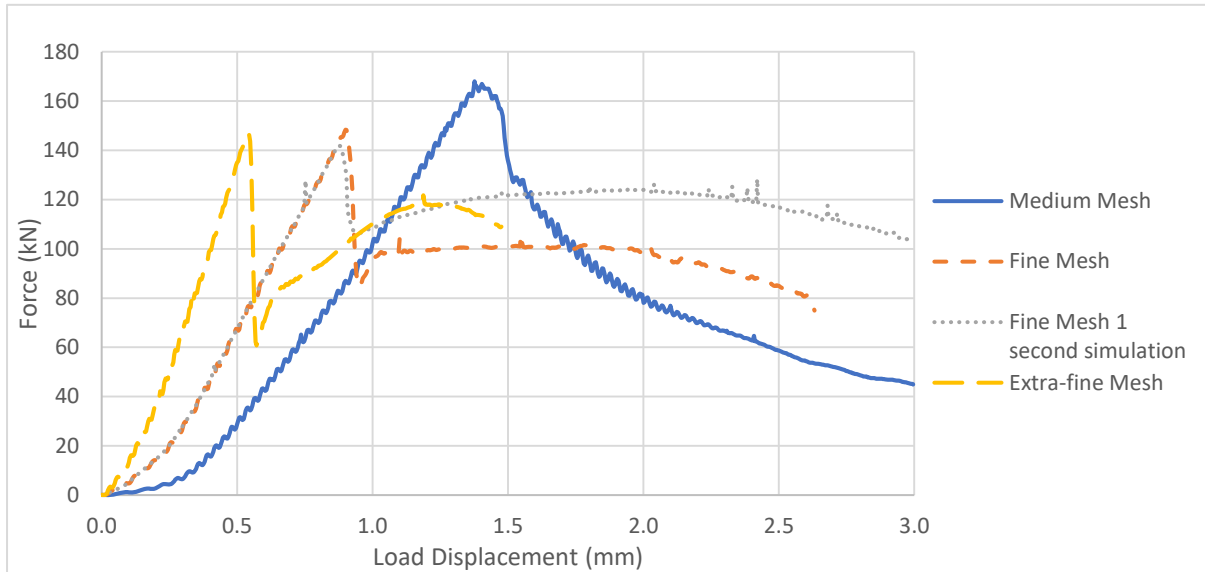


Figure 32: Validation Splitting Test Simulation force vs displacement results with different mesh sizes

5.3.3 Discussion

5.3.3.1 General Loading Response

The loading force vs displacement response for each mesh shown in Figure 32 shows the similarity in general response patterns for each. The simulations were run until either the 3×10^{-3} m strip displacement had been reached or until the simulation became unstable due to widespread failure and stopped. The coarse mesh is not included in this figure as it was too coarse to give a reliable response in this specific test and would obscure the other results. However, the crack pattern is included as it still shows the splitting concept of the test.

All the included responses curve at the beginning as the bearing strips compress and the simulation finds contact across the surface. Then they rise linearly to a maximum load, corresponding to a similar tensile stress value specified in the input parameters. Sudden failure and crack opening takes place and the load drops. In the finer meshes, the load begins to rise again but then falls towards failure. All meshes generally demonstrate the type of failure response expected from typical concrete samples. For example, they can be compared with the experimental specimens tested and furthermore, samples tested in Rocco et al (1998). In a way, the model is solution verified in that the responses do make sense however many mesh dependent features can be observed and these have to be accounted for.

5.3.3.1.1 Mesh Dependent Features

The rate at which the load rises is slower and the displacement at failure is higher for coarser meshes. Initially, the loading strip finds the contact of the cylindrical mesh slower because the

mesh is made up of many straight lines essentially. With the strips modelled as shells, the thickness is constant therefore, the even displacement of the strip creates a flat edge on the cylinder. If the strip lands on a point, the element below must strain before contact with a flatter surface is made. After that, the load rises more slowly potentially because the coarser meshes smear the loading effects more as opposed to allowing for higher stresses to concentrate on single smaller elements. The larger elements must be deformed significantly more to induce the same strain which means that lower stresses in these elements exist for longer and the total load takes longer to rise. The test relies on the formation of compressive stresses to induce tensile stresses and as soon as the stresses in the central crack formation reach the failure stress, the specimen then fails. If the compressive stresses are lower then the tensile stresses will also most likely be lower so this could be why the load rises more slowly and plate displacement is higher at failure.

After cracking, a different response is observed as the mesh gets coarser. The medium mesh continues to curve downwards heading for an asymptotic meeting with the zero stress axis while the finer meshes undergo a reloading pattern towards a more unstable failure. In coarser meshes, the area of failed material as the crack finally forms is one element wide. No load is transmitted to the base through this element so in the medium mesh for instance, the area the load can continue to pass vertically through from the strips is very small and hence, it continues to curve downwards at the end of the simulation as may be anticipated in standard tensile splitting tests. In the finer meshes, the width of one element is much smaller and so the load from the loading strips can continue to travel round the failed area more efficiently. The loading area does not decrease enough compared to the loading from the strip displacement so this causes the reaction load to rise again. The finer the mesh, the more extreme this behaviour is.

Given that the failures in the permeable concrete simulations occurred too quickly, these results show that this was more due to the mesh size chosen. Choosing a coarser mesh could make the pre-peak loading more consistent with the experimental observations however that could risk obscuring the post-peak response even more.

5.3.3.1.2 Time Dependent Features

The 1 second simulation uses the fine mesh and was implemented to prove that applying the load more slowly would not change the overall response behaviour. With a faster loading application, dynamic force effects can propagate through the material and cause the response to not be consistent with a fully static test. As can be seen in Figure 32, the longer application time does smooth out the failure response and allows a higher load to be carried after failure. However, the failure displacement, initial loading rate and general response post-peak still follow the same behavioural patterns. The test is still time dependent for the small timespans used as the paths do not match to a certain degree but since observed behaviour is very similar and experimental samples show greater variation than this, the model is still useful for determining a reasonable

predicted response. Therefore, the shorter test is still valid within the high degree of uncertainty found in the experiments.

5.3.3.2 Crack Patterns

The crack patterns produced by the simulation were also analysed to ensure that failure would take place through the same predicted modes. These are shown in Figure 33. The patterns were taken from the first frame after the occurrence of cracking failure and show significant strains in the material that would relate to crack opening. As can be seen, the shape, the position and the nature of the crack boundaries are very similar in all simulations. The tensile cracks are thinner towards the middle and the area of significant strain widens into a wedge shape towards the loading strips where crushing is occurring. This shows that the crack opening mechanism observed in the permeable concrete simulation is not mesh dependent in terms of the shape.

5.3.3.3 Conversion Factor Calculation

Over the four responses shown in Figure 32, the maximum force converges to a value of around 148 kN which converts to a predicted tensile splitting test strength, $f_{t,sp}$, of 2.1 MPa. The input uniaxial tensile strength specified by **FT** was 2.4 MPa so it is clear that a conversion factor was produced, as predicted by Malárics & Müller (2010). Given that the extra-fine mesh took considerably longer to complete, even for the shorter loading time simulated, the fine mesh was selected for use in the permeable concrete simulations as it produced a maximum stress that was very similar to the extra-fine mesh result. The ratio between the input tensile stress and the output splitting tensile stress was calculated using formula (2) as:

$$\alpha_{sp} = \frac{f_t}{f_{t,sp}} = \frac{2.4}{2.1} = 1.143$$

This was used as the conversion factor to convert the splitting tensile strengths predicted by the experimental samples into the input uniaxial tensile strength parameter **FT** for each permeable concrete simulation set, as mentioned in section 5.1.1.

5.3.4 Validation and Objectivity Results Summary

Due to mesh geometry contact and element size, the model is clearly mesh dependent although each mesh's response is reasonable. Time dependency is more visible in the post-peak regime however it is relatively insignificant as the pre-peak response and overall behaviour is much the same for both timescales simulated. The crack patterns are not mesh dependent as they each follow a similar path and show the same features. The only difference is the time at which the main cracking failure occurs.

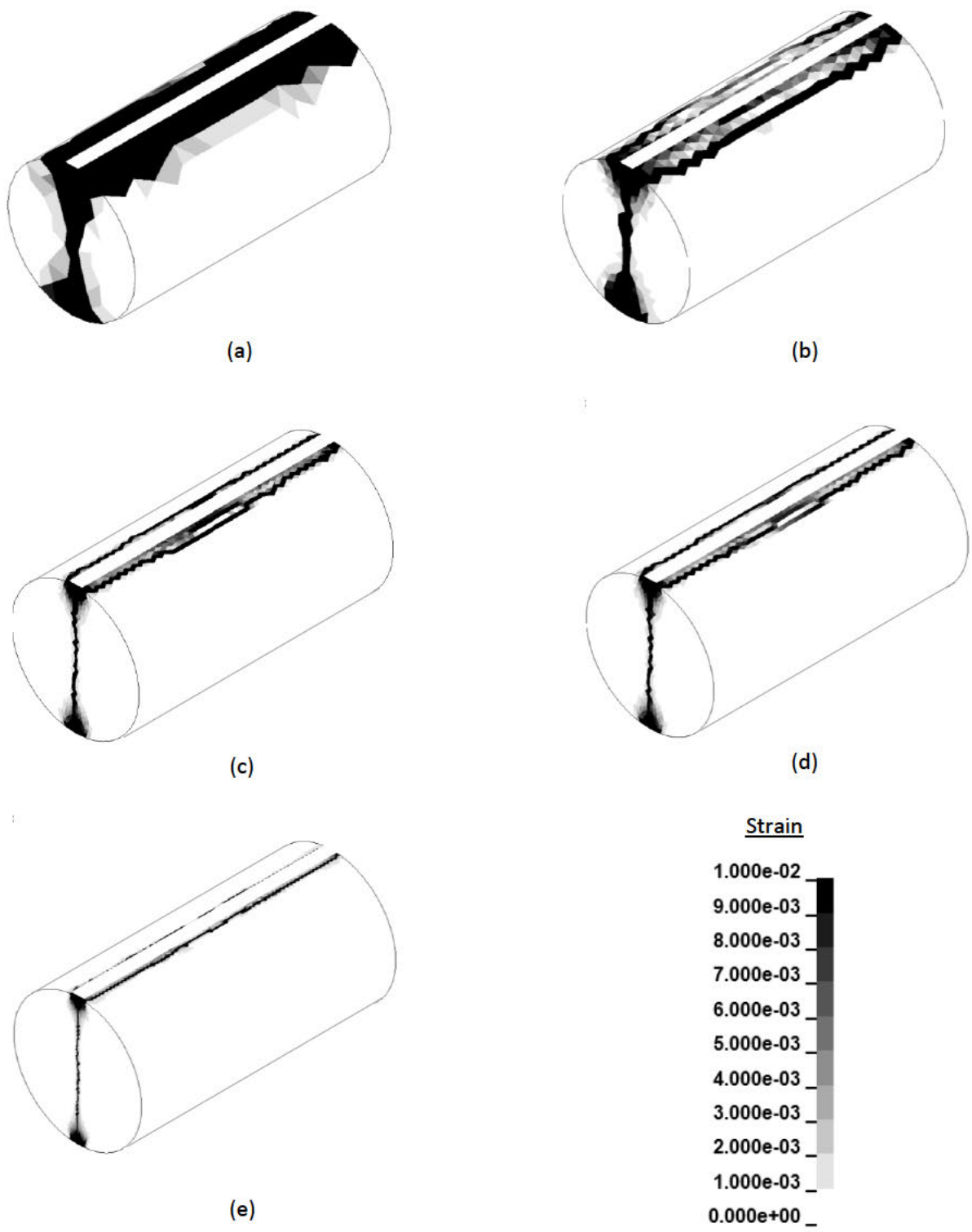


Figure 33: LS-DYNA simulated crack patterns in a standard tensile splitting test for the (a) coarse mesh, (b) medium mesh, (c) fine mesh, (d) 1 second simulation fine mesh, (e) extra-fine mesh

6 Results in Relation to Permeability Investigation

While it has been shown in the experiments in section 3.4 that the relevant measurable mechanical properties have been improved, the porosity and overall permeability of each set was also investigated and can be read in detail in Conneely (2019).

6.1 Results

A summary of the main permeability results is presented here and combined with the compressive and tensile strength of the concrete in Table 13, Figure 34 and Figure 35, to gain an overall picture of the influence of the steel fibres.

Table 13: Strength and Permeability results summary for each concrete set

Set	Compressive Strength (MPa)	Splitting Test Tensile Strength (MPa)	Conversion Factor	Uniaxial Tensile Strength Predicted (MPa)	Average Permeability (cm/s)
1	8.53	1.14	1.143	1.30	0.552
2	18.82	1.41		1.61	0.208
3	15.03	1.34		1.53	0.595
4	26.78	1.92		2.19	0.238

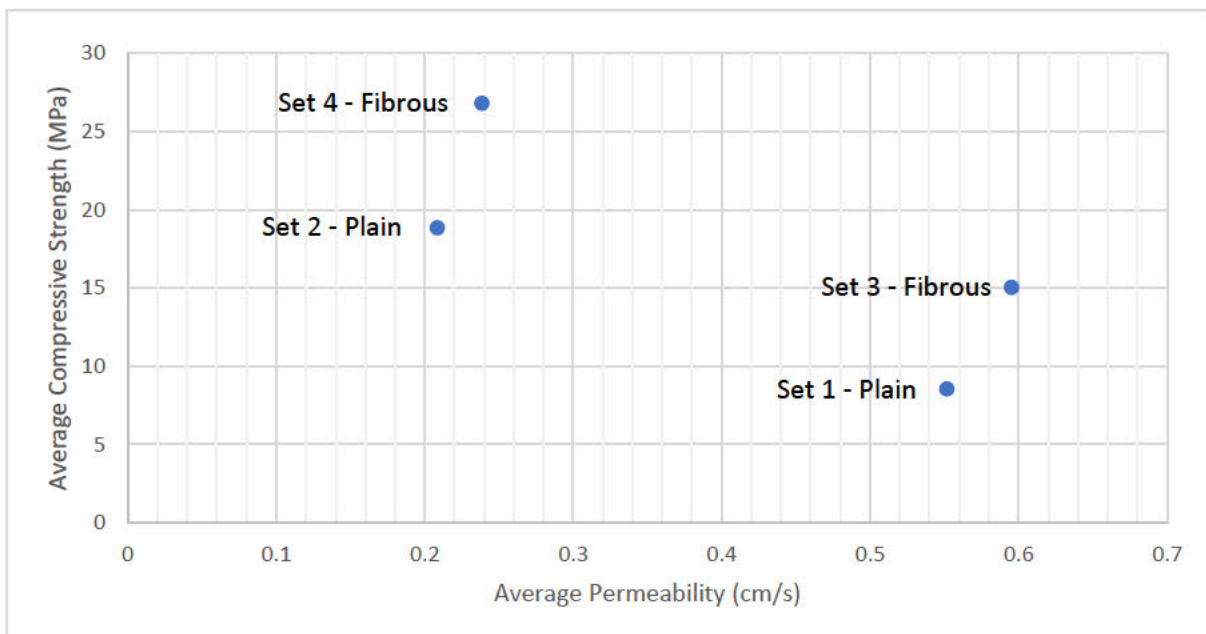


Figure 34: Compressive Strength vs Permeability results summary

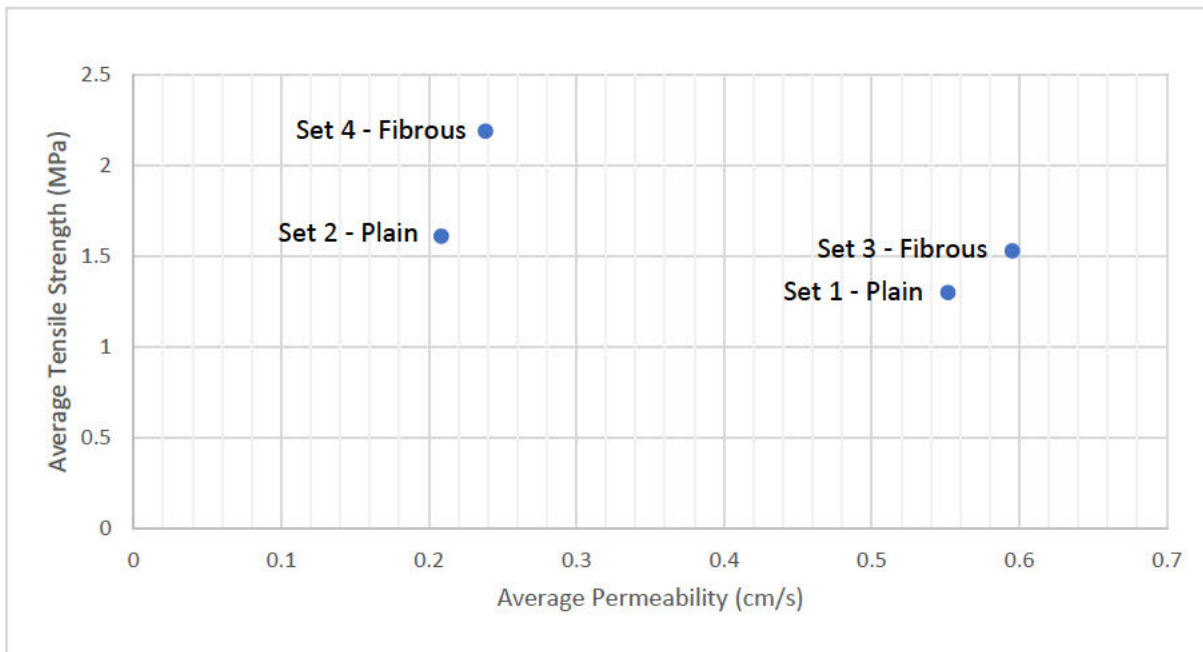


Figure 35: Tensile Strength vs Permeability results summary

6.2 Discussion

What can be seen clearly from Figures 34 and 35 is that rather than decrease the permeability by lowering porosity slightly, which is what may be expected, the fibres are consistently shown to increase the permeability. The permeability is increased more for the 20 mm samples (Set 1 and 3) in absolute value but as a relative value, the increase is only 8% whereas the 10 mm samples (Set 2 and 4) show a permeability increase of over 14%. These results suggest that the fibres are causing small gaps and connecting voids between the aggregates and this allows the water to find easier routes through. This effect does not significantly affect the density of the concrete as the fibrous samples are still denser than the plain samples.

The overall outcome from this analysis is that the permeability is not hindered by the presence of fibres while the main mechanical properties are improved as well. In terms of the uses and potential of permeable concrete, the inclusion of fibres appears to be beneficial for its main water-shedding purposes and possible extension into more mechanical applications.

7 Conclusions

The overall purpose of this study has been to determine whether the mechanical properties of permeable concrete mixes could be improved without severely adversely affecting the permeability. This project has focussed on the change in mechanical properties induced by the addition of steel fibres.

Different mixes of plain and fibrous permeable concrete have been experimentally tested through compression and tensile splitting tests. It has been found that samples with fibres had significantly increased compressive strength, slightly increased tensile strength and a small increase in stiffness. Resistance to crumbling was also improved. However, it is recommended that further samples are tested to confirm the degree of improvement as the spread of some results was quite wide. It has also been determined that a different type of tensile test would be required to determine all of the effects caused by the fibres (see Further Work below) as post-peak tensile behaviour could not be studied fully.

Single element simulations have then been performed to confirm behavioural parameters for the mixes against the experimental results. Then, the tensile splitting test has been modelled for each mix using a homogeneous mesh and the CDPM2 concrete behaviour model to determine the applicability of this method for future applications. In the single element tests, it has been determined that the behaviour model performed well generally against the experimental compression results within the displacement range tested. From the splitting test simulation, it became clear that a reasonable prediction of the splitting test pre-peak behaviour and splitting test strength could be gained. Therefore, the uniaxial tensile strength could also be roughly determined as well with the conversion factor close to unity. Accuracy of tensile post-peak parameters could not be explored properly in the simulation due to the use of the splitting test and responses generally did not always represent experimental results well, although similar failure patterns appeared in each. There is potential for more effective use of this model and mesh combination in uniaxial tensile applications since the fibres held samples together in the experimental splitting tests as they would with conventional concrete. Behaviour in the uniaxial mode may therefore be relatively similar but with no dilution from other physical processes.

The overall project did not rely on the results of the simulations, only the experiments. The main results of Conneely (2019) have been combined with results from this investigation and it has been shown that not only did the fibres improve mechanical performance, the permeability also increased as well, leading to a complete improvement in overall concrete behaviour. This suggests that the introduction of fibres into permeable concrete mixes could be highly beneficial, especially for the flexibility and efficiency of future uses.

8 Further Work

This section specifically refers to the mechanical properties part of the investigation.

What has been understood through these experiments is that the tensile behaviour of the sample before the peak load has been well investigated and results show that the simulation model could describe the general pre-cracking experimental pattern reasonably well. What needs to be investigated further is the post-peak behaviour that cannot be accurately described by a tensile splitting test. A uniaxial tension test would be more appropriate for the types of model testing desired and in general for the exploration of post-peak behaviour. A direct measurement of the uniaxial tensile stress required for a material sample to fail would be far more valuable than making assumptions based on simplified mesh simulations and furthermore, the post-peak response, in relation to the ductility and crack opening, is required to allow the material model to be refined accurately. While this is more awkward than the splitting test, hence the reason for not undertaking it originally, the confidence in the results would rise sufficiently for this to be worth the cost. A 3-point bending test could also be employed for this purpose however the complex nature of the material may not make it as desirable.

Regarding measurement methods, the camera setup employed could not realistically or visibly describe the tiny deformations observed before or during failure and so was mostly obsolete, aside from macroscopic measurements. To help accurately determine very small strains and cracking in the material to inform the behaviour description, some form of strain gauge or digital image correlation would be recommended. These methods would also be effective with the uniaxial test where failure and fracture modes are more reliable and directly measurable.

The steel fibres within the concrete are a potential source of further research. In normal fibre reinforced concrete, water cannot get access to the fibres as the material is relatively impermeable. Now, as they are deliberately placed in a material designed to pass water through it, any uncovered areas may be liable to corrode over time. This will likely have an effect on the material response and potentially create zones of weakness in the material. A long-term study on the effects of water in steel fibre permeable concrete could be key to understanding potential use limitations and advantages of other fibre types.

9 References

- AmBrSoft development (2014), AmBrSoft.com [online] "Materials Density Table", Available: http://www.ambrsoft.com/calcpysics/density/table_2.htm [7 Jan 2019]
- ASTM International, (2017) "Standard Test Method for Splitting Tensile Strength of Cylindrical Concrete Specimens", C496/C496M-17, pp. 2-4
- Babuska, I. and Oden, T. (2004) "Verification and validation in computational engineering and science: basic concepts", Computer methods in applied mechanics and engineering [Electronic] vol. 193, pp. 2. Available: http://users.ices.utexas.edu/~oden/Dr._Oden_Reprints/2004-004.verification_and.pdf [5 Jan 2019]
- Bažant, Z. and Oh, B. (1983) "Microplane Model for Fracture Analysis of Concrete Structures", The 'Technological Institute' Northwestern University, Evanston, Illinois, USA
- Bekaert (2018) "Dramix® 3D 6535BG", [Electronic] Available: http://www.s-w.co.il/_Uploads/dbsAttachedFiles/3D_6535BG.pdf [5 Jan 2019]
- Bright, N. and Roberts, J. (2010) "Structural Eurocodes: Extracts from the Structural Eurocodes for Students of Structural Design", 3rd Edition, London: BSI, pp. "1-9", "2-18"
- British Standards Institution (2012) "*Testing hardened concrete Part 1: Shape, dimensions and other requirements for specimens and moulds*", BS EN 12390-1:2012, London: BSI, pp. 6-7
- British Standards Institution (2009) "*Testing hardened concrete Part 3: Compressive Strength of Test Specimens*", BS EN 12390-3: 2009, London: BSI, pp. 6-10
- British Standards Institution (2009) "*Testing hardened concrete Part 6: Tensile splitting strength of test specimens*", BS EN 12390-6:2009, London: BSI, pp. 6-11
- Cai, Z. and Ross, R. (2010) "Mechanical Properties of Wood-Based Composite Materials", Wood Handbook, Chapter 12 [Electronic] Wisconsin: Forest Products Laboratory, pp. "12-4". Available: https://www.fpl.fs.fed.us/documnts/fplgrtr/fplgrtr190/chapter_12.pdf [5 Jan 2019]
- Care, F. Subagio, B and Rahman, H. (2018) "Porous concrete basic property criteria as rigid pavement base layer in Indonesia", MATEC Web of Conferences [Electronic] vol. 147, EDP Sciences, pp. 5. Available: https://www.matec-conferences.org/articles/matecconf/abs/2018/06/matecconf_sibe2018_02008/matecconf_sibe2018_02008.html [5 Jan 2019]

- Carol, I. Rizzi, E. Willam, K (1999) "On the formulation of anisotropic elastic degradation. I. Theory based on a pseudo-logarithmic damage tensor rate", *International Journal of Solids and Structures* [Electronic] vol. 38, no. 4, pp. 491-518. Available: <https://www.sciencedirect.com/science/article/pii/S0020768300000305> [5 Jan 2019]
- CEB-FIP (2010) "CEB-FIP Model Code 2010", *fib Bulletin* 65, vol.1, pp.76-81
- Chen, W. (2007) "Plasticity in Reinforced Concrete", J. Ross Publishing, pp. 20-39
- Conneely, G.M. (2019) "Pervious Concrete for Sustainable Construction: Experiments on the effect of aggregate size and steel fibres on permeability", MEng Thesis, University of Glasgow, Glasgow, Scotland.
- Deo, O. and Neithalath, N. (2010) "Compressive Behaviour of Pervious Concretes and a Quantification of the Influence of Random Pore Structure Features", *Materials Science and Engineering A* [Electronic] vol. 528 pp. 402-412. Available: <https://www.sciencedirect.com/science/article/abs/pii/S0921509310010543> [5 Jan 2019]
- Grassl, P. (2016) "User manual for MAT_CDPM (MAT_273) in LS-DYNA" [Electronic] Available: <http://petergrassl.com/Research/DamagePlasticity/CDPMLSDYNA/index.html> [15 Dec 2018]
- Grassl, P. (2017) petergrassl.com [online] "MAT_CDPM (MAT_273) in LS-DYNA". Available: <https://petergrassl.com/Research/DamagePlasticity/CDPMLSDYNA/index.html#Input> [8 Jan 2019]
- Grassl, P. and Jirásek, M. (2006) "Damage Plastic Model for Concrete Failure", *International Journal of Solids and Structures*, vol. 43, pp. 7166-7194
- Grassl, P. Xenos, D. Nyström, U. Rempling, R. Gylltoft, K. (2013) "CDPM2: A damage plasticity approach to modelling the failure of concrete", *International Journal of Solids and Structures* [Electronic] vol. 50, no. 24, pp. 3805-3816. Available: <http://www.sciencedirect.com/science/article/pii/S0020768313002886> [5 Jan 2019]
- Jirásek, M. and Bažant, Z. (2002) "Inelastic Analysis of Structures", Wiley pp. 358, 365
- Joshi, T. Dave, U. (2016) "Evaluation of strength, permeability and void ratio of pervious concrete with changing w/c ratio and aggregate size", *International Journal of Civil Engineering and Technology* [Electronic] vol. 7, no. 4, pp. 276–284. Available: http://www.iaeme.com/MasterAdmin/uploadfolder/IJCIET_07_04_023/IJCIET_07_04_023.pdf [5 Jan 2019]
- Ju, J.W. (1989) "On energy-based coupled elastoplastic damage theories: Constitutive modeling and computational aspects", *International Journal of Solids and Structures* [Electronic] vol. 25, no. 7, pp. 803-833. Available: <https://www.sciencedirect.com/science/article/pii/0020768389900152> [5 Jan 2019]

- Kachanov, L.M. (1958) "Time rupture process under creep conditions", Izv. Akad. Nauk SSR
- Kretschmann, D. (2010) "Mechanical Properties of Wood", Wood Handbook, Chapter 5 [Electronic] Wisconsin: Forest Products Laboratory, pp. "5-3". Available: https://www.fpl.fs.fed.us/documnts/fplgtr/fplgtr190/chapter_12.pdf [5 Jan 2019]
- Livermore Software Technology Corporation (2006) "LS-DYNA Theory manual" [Electronic] Available: <http://www.lstc.com/download/manuals> [5 Jan 2019]
- Lockhart, E. (2017) "Modelling the Failure of Reinforced Concrete Subjected to Dynamic Loading Using CDPM2 in LS-DYNA", MEng Thesis, University of Glasgow, Glasgow, Scotland.
- Mahalingam, R. Mahalingam, S. (2016) "Analysis of pervious concrete properties", Građevinar vol. 68, no. 6, pp. 493-501. Available: <http://casopis-gradjevinar.hr/assets/Uploads/JCE-68-2016-6-5-1434-EN.pdf> [5 Jan 2019]
- Malárics, V. and Müller, H.S. (2010), "Evaluation of the splitting tension test for concrete from a fracture mechanical point of view", Fracture Mechanics of Concrete and Concrete Structures Assessment, Durability, Monitoring and Retrofitting of Concrete Structures, Korea Concrete Institute, Seoul, pp. 709-715
- McTaggart, S. (2016) "LS-DYNA for Analysing the Failure of Concrete Structures" MEng Thesis, University of Glasgow, Glasgow, Scotland.
- Menetrey, P. and Willam, K.J. (1995) "Triaxial failure criterion for concrete and its generalization", ACI Structural Journal Volume vol. 92, no. 3, pp. 311-318
- Middlemiss, J. (2019) "The influence of steel fibres on the strength and deformation capacity of reinforced concrete connections using nonlinear finite element analyses", MEng Thesis, University of Glasgow, Glasgow, Scotland.
- Naaman, A. (1987) "High performance fiber reinforced cement composites", IABSE reports, pp. 372-375
- Naik, T.R. Kumar, R. Ramme, B.W. Canpolat, F. (2012) "Development of High-Strength, Economical Self-Consolidating Concrete", Construction and Building Materials [Electronic] vol. 30 pp. 463-469. Available: <https://www.sciencedirect.com/science/article/abs/pii/S0950061811007021> [5 Jan 2019]
- Nemanti, M. (2015) "Aggregates for Concrete", [Electronic] University of Washington, Seattle, Washington, USA. Available: <http://courses.washington.edu/cm425/aggregate.pdf> [7 Jan 2019]
- Neset, J. and Skoglund, S. (2007) "Reinforced Concrete Subjected to Restraint Forces", Master's Thesis, Chalmers University of Technology, Göteborg, Sweden.

- Paliwal, B. Hammi, Y. Moser, R.D. Horstemayer, M.F (2017) "A three-invariant cap-plasticity damage model for cementitious materials", International Journal of Solids and Structures [Electronic] vol. 108, pp. 186–202 Available: <https://www.sciencedirect.com/science/article/pii/S0020768316303894> [5 Jan 2019]
- Reddy, J.N. (2015) "An Introduction to Nonlinear Finite Element Analysis", 2nd Edition, Oxford University Press pp. 7-8
- Rehder, B. Kingsten, B. and Neithalath, N. (2014) "Fracture behavior of pervious concretes: The effects of pore structure and fibers", Engineering Fracture Mechanics [Electronic] vol. 118, Elsevier Ltd, pp. 6-12. Available: <https://www.sciencedirect.com/science/article/pii/S0013794414000253> [5 Jan 2019]
- Rocco, C. Guinea, G.V. Planas, J. Elices, M (1998) "Experimental analysis of rupture mechanisms in the Brazilian test", Fracture Mechanics of Concrete Structures, Freiburg, Germany: AEDIFICATIO Publishers, pp. 121-130
- Schlaich, J. and Schäfer, K. (1991) "Design and detailing of structural concrete using strut-and-tie models", The Structural Engineer [Electronic] vol. 69, no.6, pp. 113-124 Available: http://www.pgmech.ime.eb.br/~webde2/prof/ethomaz/bloco_sobre_estacas/biela_tirante.pdf [5 Jan 2019]
- Shahriar, S. Civil Today [online] "Density of Aggregate - Bulk and Relative Density". Available: <https://civiltoday.com/civil-engineering-materials/aggregate/198-density-of-aggregate> [7 Jan 2019]
- Siddiquee, T. Civil Today [online] "Specific Gravity of Cement - Details & Test Procedure". Available: <https://civiltoday.com/civil-engineering-materials/cement/120-specific-gravity-of-cement-definition-meaning-calculation-test-procedure> [7 Jan 2019]
- Sun, J.S. Lee, K.H. and Lee H.P. (1999), "Comparison of implicit and explicit Finite element methods for dynamic problems", Journal of Materials Processing Technology [Electronic] vol.105, Department of Mechanical and Production Engineering, National University of Singapore, pp. 110-118. Available: <https://www.sciencedirect.com/science/article/pii/S092401360000580X> [5 Jan 2019]
- Tennis, P. Lemming, M and Akers, D. (2004) "Pervious Concrete Pavements", [Electronic] 2nd Edition, Portland Cement Association, pp. 1-8. Available: http://myscmap.sc.gov/marine/NERR/pdf/PerviousConcrete_pavements.pdf [5 Jan 2019]

10 Appendices

Appendix A - Concrete Constituent Calculations

Concrete Volume for each set

3 cubes and 6 cylinders required for each concrete set.

Cube size = $100 \times 100 \times 100 \text{ mm} = 0.1 \times 0.1 \times 0.1 \text{ m}$

Volume required for 3 cubes = $0.1^3 \times 3 = 0.003 \text{ m}^3$

Cylinder size = $\emptyset 150 \times 300 \text{ mm} = \emptyset 0.15 \times 0.3 \text{ m}$

Volume required for 6 cylinders = $\pi \times \left(\frac{0.15}{2}\right)^2 \times 0.3 \times 6 = 0.03181 \text{ m}^3$

Sub – total = $0.003 + 0.03181 = 0.03481 \text{ m}^3$

Adding 15% for spillages and 2% for trials = 17%

Total volume for each mix = $0.03481 \times 1.17 = \mathbf{0.04073 \text{ m}^3}$

Set materials

1	2	3	4
20 mm aggregate	10 mm aggregate	20 mm aggregate	10 mm aggregate
Cement	Cement	Cement	Cement
Water	Water	Water	Water
		Steel fibres	Steel fibres

Materials Required	Specific Gravity (Source)	Bulk Density (Source) kg/m ³
20 mm aggregate	2.65 (Shahriar)	1550 (estimated from Nemanti, 2015)
10 mm aggregate		1600 (estimated from Nemanti, 2015)
Cement	3.15 (Siddiquee)	-
Water	1.00 (Standard)	-
Steel Fibres	7.85 (AmBrSoft, 2014)	-

Material/m³ Required

Set 1

Material Maximum Theoretical Densities (Specific Gravity x Density of Water)

Cement	3150 kg/m ³
Aggregate	2650 kg/m ³
Water	1000 kg/m ³

Materials/m³ in bulk density

20 mm aggregate: **1550 kg**
(assuming bulk density is density in mix)

Aggregate:Cement ratio, 4.0->4.5 range
Use 4.2 (Tennis et al, 2004)

Cement: $\frac{1550}{4.2} = \mathbf{369\ kg}$

Water:Cement Ratio around 0.3
(Tennis et al, 2004)

Water: $369 \times 0.3 = \mathbf{111\ kg}$

Checking void content (Joshi and Dave (2016)) - Aiming for between 15% and 25%

$$\text{Void Content \%} = \left(\frac{T-D}{T} \right) \times 100$$

$$D = \frac{M_c - M_m}{V_m} \text{ (actual material density)}$$

$$T = \frac{M_s}{V_s} \text{ (maximum theoretical density)}$$

M_c - Mass of concrete (kg)

M_s - Mass of solid material per m³ of concrete(kg/m³)

M_m - Mass of mould (kg)

V_s - Volume of solid material per m³ of concrete (m³/m³)

V_m - Volume of mould (m³)

Assume $D = M_s$

$$M_s = 1550 + 369 + 111 = \mathbf{2030\ kg/m^3} \text{ (target density)}$$

$$V_s = \frac{1550}{2650} + \frac{369}{3150} + \frac{111}{1000} = 0.585 + 0.117 + 0.111 = 0.813\ m^3/m^3$$

$$T = \frac{2030}{0.813} = 2497\ kg/m^3$$

$$\text{Void Content \%} = \left(\frac{2497-2030}{2497} \right) \times 100 = \mathbf{18.7\%}$$

Set 2

Materials/m³ in bulk density

10 mm aggregate: **1600 kg**
(assuming bulk density is density in mix)

Aggregate:Cement ratio, 4.0->4.5 range
Use 4.2 (Tennis et al, 2004)

Cement: $\frac{1600}{4.2} = \mathbf{381\ kg}$

Water:Cement Ratio around 0.3
(Tennis et al, 2004)

Water: $381 \times 0.3 = \mathbf{114\ kg}$

Checking void content (Joshi and Dave (2016)) - Aiming for between 15% and 25%

$M_s = 1600 + 381 + 114 = \mathbf{2095\ kg/m^3}$ (target density)

$$V_s = \frac{1600}{2650} + \frac{381}{3150} + \frac{114}{1000} = 0.604 + 0.121 + 0.114 = 0.839\ m^3/m^3$$

$$T = \frac{2095}{0.839} = 2497\ kg/m^3$$

$$\text{Void Content \%} = \left(\frac{2497 - 2095}{2497} \right) \times 100 = \mathbf{16.1\%}$$

Set 3

Same material amounts used as for Set 1 but with the addition of 0.5% volume of fibres.

Steel Density (Specific Gravity x Density of Water): 7850 kg/m³

Weight of fibres/m³ = %vol × Volume of concrete × Density

$$\text{Weight of fibres/m}^3 = \frac{0.5}{100} \times 1 \times 7850 = 39.25\ kg/m^3$$

Set 4

Same material amounts used as for Set 2 but with the addition of 0.5% volume of fibres (same as set 3).

Materials required for each set with volume of 0.04073m³

Set 1: $20\text{ mm agg.} = 1550 \times 0.04073 = 63.13\text{ kg} \approx 63\text{ kg}$

$Cement = 369 \times 0.04073 = 15.03\text{ kg} \approx 15\text{ kg}$

$Water = 111 \times 0.04073 = 4.52\text{ kg} \approx 4.5\text{ kg}$

Set 2: $20\text{ mm agg.} = 1600 \times 0.04073 = 65.17\text{ kg} \approx 65\text{ kg}$

$Cement = 381 \times 0.04073 = 15.52\text{ kg} \approx 15.5\text{ kg}$

$Water = 114 \times 0.04073 = 4.64\text{ kg} \approx 4.6\text{ kg}$

Set 3: $20\text{ mm agg.} \approx 63\text{ kg}$

$Cement \approx 15\text{ kg}$

$Water \approx 4.5\text{ kg}$

$Steel\ Fibres = 39.25 \times 0.04073 \approx 1.6\text{ kg}$

Set 4: $20\text{ mm agg.} \approx 65\text{ kg}$

$Cement \approx 15.5\text{ kg}$

$Water \approx 4.6\text{ kg}$

$Steel\ Fibres \approx 1.6\text{ kg}$


```

*DATABASE_NODFOR
$      dt
  &TASCII
*DATABASE_NODOUT
$      dt
  &TASCII
*DATABASE_SPCFORC
$#     dt
  &TASCII
$---+---1---+---2---+---3---+---4---+---5---+---6---+---7---+---8
*DATABASE_BINARY D3PLOT
$      dt
  &TDplot
$
*DATABASE_HISTORY_NODE
$Displacement node
5
$
*DATABASE HISTORY NODE
$Displacement node
6
$
*DATABASE_HISTORY_NODE
$Displacement node
7
$
*DATABASE HISTORY NODE
$Displacement node
8
$
*DATABASE_HISTORY_NODE
$Displacement node
9
$
*DATABASE HISTORY NODE
$Displacement node
10
$
*DATABASE_HISTORY_NODE
$Displacement node
11
$
*DATABASE HISTORY NODE
$Displacement node
12
$
*DATABASE HISTORY NODE
$Displacement node
13
$
*DATABASE_HISTORY_NODE
$Displacement node
14
$
$---+---1---+---2---+---3---+---4---+---5---+---6---+---7---+---8
*DATABASE_EXTENT_BINARY
$  neiph  neips  maxint  strflg  sigflg  epsflg  rltflg  engflg
   5      5      1      1      1
$  cmpflg  ieverp  beamip
   0
$---+---1---+---2---+---3---+---4---+---5---+---6---+---7---+---8
$
$
*SECTION_SOLID
$permconcrete
$#  secid  elform  aet
   1     10     0
$
$
*SECTION_Shell
$stopandbottomplates
$  SECID  ElForm  SHRF  NIP  PROPT  QR/IRID  ICOMP  SETYP
   2      2      0
$---+---1---+---2---+---3---+---4---+---5---+---6---+---7---+---8
$  T1     T2     T3     T4     NLOC  MAREA  IDOF  EDGSET
  0.004  0.004  0.004  0.004
$

```

```

$
*Include
s1material.k
$
*BOUNDARY SPC SET
$---+---1---+---2---+---3---+---4---+---5---+---6---+---7---+---8
$   SID      CID      DOFX      DOFY      DOFZ      DOFRX      DOFRY      DOFRZ
$       1         0         1         1         1         1         1         1
$
$
*BOUNDARY SPC SET
$---+---1---+---2---+---3---+---4---+---5---+---6---+---7---+---8
$   SID      CID      DOFX      DOFY      DOFZ      DOFRX      DOFRY      DOFRZ
$       2         0         1         1         1         1         1         1
$
$
*Boundary_Prescribed_Motion_Set
$---+---1---+---2---+---3---+---4---+---5---+---6---+---7---+---8
$   ID      DOF      VAD      LCID      SF      VID      DEATH      BIRTH
$       2       3       2      111     -1.0     1         1         1
$
$ applied Y-direction displacement
*DEFINE_CURVE
111, 0, 1., 1., 0., 0.
0.0, 0.0
&Tend, &MaxDisp
&Tend2, &MaxDisp
$
$ maximum time increment
*DEFINE CURVE
9,0,1.,1.,0.,0.
0.0, &DtMax
&Tend, &DtMax
&Tend2, &DtMax
$
*Include
fincylp.k
$
*Include
fineShellPlates.k
$
$
*CONTACT AUTOMATIC SURFACE TO SURFACE ID
$---+---1---+---2---+---3---+---4---+---5---+---6---+---7---+---8
$#  cid      |      |      |      |      |      |      |      |
$       1         |         |         |         |         |         |         |
$                                     Plates to cylinder contact
$---+---1---+---2---+---3---+---4---+---5---+---6---+---7---+---8
$   |      |      |      |      |      |      |      |
$   ssid  msid  sstyp  mstyp  sboxid  mboxid  spr  mpr
$   601    1     3       3       3       3       3
$---+---1---+---2---+---3---+---4---+---5---+---6---+---7---+---8
$   |      |      |      |      |      |      |      |
$   fs    fd    dc    vc    vdc  penchk  bt    dt
$   0.1
$---+---1---+---2---+---3---+---4---+---5---+---6---+---7---+---8
$   |      |      |      |      |      |      |      |
$   sfs   sfm   sst   mst   sfst  sfmt   fsf   vsf
$           4.0E-3
$
*END

```

Variations of this input file were used for all sets simulated including the validation set with the material and cylinder meshes changing accordingly.

B.2 - Cylinder Mesh Input File

All cylinder mesh variations were generated from this base file using the T3D program. Different element sizes were specified in the conversion from the input to the output file.

```
#FRP concrete cylinder with height=0.3 m and diameter=0.15 m

vertex 1 xyz 0.0 0.0 0.075
vertex 2 xyz 0.300 0.0 0.075
vertex 3 xyz 0.0 0.150 0.075
vertex 4 xyz 0.300 0.150 0.075

#data points
vertex 5 xyz 0.0 0.0525 0.075
vertex 6 xyz 0.0 0.0975 0.075
vertex 7 xyz 0.075 0.0525 0.075
vertex 8 xyz 0.075 0.0975 0.075
vertex 9 xyz 0.15 0.0525 0.075
vertex 10 xyz 0.15 0.0975 0.075
vertex 11 xyz 0.225 0.0525 0.075
vertex 12 xyz 0.225 0.0975 0.075
vertex 13 xyz 0.3 0.0525 0.075
vertex 14 xyz 0.3 0.0975 0.075

curve 101 order 4 vertex 1 3
polygon 1 xyz 0.0 0.0 0.225 weight 0.3333333
polygon 2 xyz 0.0 0.150 0.225 weight 0.3333333
curve 102 order 4 vertex 1 3
polygon 1 xyz 0.0 0.0 -0.075 weight 0.3333333
polygon 2 xyz 0.0 0.150 -0.075 weight 0.3333333

curve 103 order 4 vertex 2 4
polygon 1 xyz 0.300 0.0 0.225 weight 0.3333333
polygon 2 xyz 0.300 0.150 0.225 weight 0.3333333
curve 104 order 4 vertex 2 4
polygon 1 xyz 0.300 0.0 -0.075 weight 0.3333333
polygon 2 xyz 0.300 0.150 -0.075 weight 0.3333333

#data point curves
curve 1 vertex 5 7
curve 2 vertex 7 9
curve 3 vertex 9 11
curve 4 vertex 11 13
curve 7 vertex 6 8
curve 8 vertex 8 10
curve 9 vertex 10 12
curve 10 vertex 12 14

curve 5 order 2 vertex 1 2
curve 6 order 2 vertex 3 4

patch 1 normal -1 0 0 boundary curve 101 -102 fixed vertex 5 fixed vertex 6
patch 2 normal -1 0 0 boundary curve 103 -104 fixed vertex 13 fixed vertex 14
surface 3 curve 101 6 103 5
surface 4 curve 102 6 104 5

region 1 boundary patch 1 -2 boundary surface 3 -4 size def fixed curve 1 fixed curve 2 fixed curve 3 fixed
curve 4 fixed curve 7 fixed curve 8 fixed curve 9 fixed curve 10
```

B.3 - Shell Loading Strips Input File

The loading strips mesh was generated using the T3D program using this input file. After generation, sets of nodes were created in LS-Prepost so that displacement loading and fixing of the loading and bearing strips respectively could be specified in the main input file.

```
# Mesh of plates. Assume 4mm shell thickness

#Bottom Support
#vertices
vertex 101 xyz 0.0 0.0675 -0.002
vertex 102 xyz 0.300 0.0675 -0.002
vertex 103 xyz 0.300 0.0825 -0.002
vertex 104 xyz 0.0 0.0825 -0.002

#Bottom Support Curves
curve 1 order 2 vertex 101 102
curve 2 order 2 vertex 102 103
curve 3 order 2 vertex 103 104
curve 4 order 2 vertex 104 101

#facets
#Bottom bottom
patch 3 normal 0 0 -1 boundary curve -1 -2 -3 -4 output yes size def
#Bottom top
patch 4 normal 0 0 1 boundary curve 1 2 3 4 output yes size def

#Top Support
#vertices
vertex 105 xyz 0.0 0.0675 0.152
vertex 106 xyz 0.300 0.0675 0.152
vertex 107 xyz 0.300 0.0825 0.152
vertex 108 xyz 0.0 0.0825 0.152

#Top Support Bottom Curves
curve 5 order 2 vertex 105 106
curve 6 order 2 vertex 106 107
curve 7 order 2 vertex 107 108
curve 8 order 2 vertex 108 105

#facets
#Top bottom
patch 9 normal 0 0 -1 boundary curve -5 -6 -7 -8 output yes size def
#Top top
patch 10 normal 0 0 1 boundary curve 5 6 7 8 output yes size def
```